

# **Resonance Treatment Using the Discrete Generalized Multigroup Method**

by

Nathan A. Gibson

B.S. Nuclear Engineering, 2010

B.S. Physics, 2010

Rensselaer Polytechnic Institute

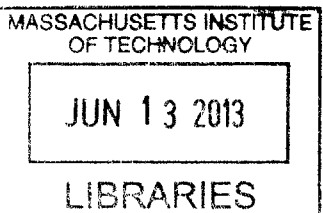
Submitted to the Department of Nuclear Science and Engineering  
in Partial Fulfillment for the Degree of

Master of Science in Nuclear Science and Engineering  
at the  
Massachusetts Institute of Technology

February 2013

© 2013 Massachusetts Institute of Technology  
All rights reserved

**ARCHIVES**



Signature of Author:

Nathan A. Gibson  
Department of Nuclear Science and Engineering  
January 18, 2013

Certified by:

Benoit Forget, Ph.D.  
Assistant Professor of Nuclear Science and Engineering  
Thesis Supervisor

Kord S. Smith, Ph.D.

KEPCO Professor of the Practice of Nuclear Science and Engineering  
Thesis Reader

Accepted by:

Mujid S. Kazimi, Ph.D.  
TEPCO Professor of Nuclear Science and Engineering  
Chair, Department Committee on Graduate Students



Resonance Treatment Using the Discrete Generalized Multigroup Method

by

Nathan A. Gibson

Submitted to the Department of Nuclear Science and Engineering on  
January 18, 2013, in Partial Fulfillment of the Requirements for the  
Degree of Master of Science in Nuclear Science and Engineering

## Abstract

In reactor physics calculations for reactor design and operations, today's methods rely on approximate models to account for resonance self-shielding effects. A multi-level approach, which includes several levels of calculations where complexity in energy is decreased as spatial complexity is increased, is employed to model nuclear reactors. However, this approach breaks down when alternate materials and reactor designs are considered. Thus, in order to simulate behavior in an unconventional system, higher fidelity methods are desired. Continuous energy or ultrafine multigroup nuclear data allows this high fidelity to be achieved but is associated with a high computational expense.

This thesis proposes that the Discrete Generalized Multigroup (DGM) method is a possible means of approximating the high fidelity results associated with an ultrafine energy mesh without the high degree of computational expense. DGM maps the ultrafine group energy mesh to a coarser energy mesh, where transport calculations are performed, through a discrete expansion. Additional data—moments of the expansion—are retained to unfold an approximate ultrafine energy spectrum. A recondensation procedure is used, where the method is applied in succession, allowing details from the coarse group calculation to influence the collapse of the coarse group data.

In applying DGM to an ultrafine energy mesh, prohibitive computational expense is seen to exist in the computation of moments of the scattering matrix and in the flux updates used to maintain stability. Means of reducing the computational expense associated with the scattering matrix are suggested, but left to future work. Flux updates are removed by introducing Krasnoselskij iteration and a group mapping algorithm to the DGM recondensation procedure. Krasnoselskij iteration allows recondensation to become convergent by using a portion of the previous iterate when updating the solution vector. The group mapping algorithm places coarse group boundaries where large disparities in fine group cross sections are present, enhancing the stability characteristics of recondensation. These algorithmic changes do not negatively impact the accuracy of the procedure and remove a large computational expense from the method. Ultimately, the method is deemed to be an attractive option for approximating a high fidelity solution.

Thesis Supervisor: Benoit Forget

Title: Assistant Professor of Nuclear Science and Engineering



# Acknowledgments

This research was performed under appointment to the Rickover Fellowship Program in Nuclear Engineering sponsored by the Naval Reactors Division of the U.S. Department of Energy.

First and foremost, I would like to express my sincerest appreciation to my thesis advisor Prof. Benoit Forget for the support, guidance, insight, and passion he has given me in my first two and a half years at MIT. In helping me select and carry out a research project, he has helped me to find my own passion in this field. I would especially like to express my gratitude for his great ability to steer my work out of the darkness when it seemed hopeless but to only gently encourage continued progress when the work was going well.

I would also like to thank my thesis reader Prof. Kord Smith, who agreed to read my thesis and lent invaluable insight even before he joined the MIT faculty. From his voice of experience, I was able to learn about current practices in the field and where my work fit into the puzzle.

Next, I would like to express my gratitude to my fellowship mentor Dr. Timothy Trumbull from the Knolls Atomic Power Laboratory. I greatly value the knowledge of nuclear data and data processing that he imparted on me throughout my Master's work. I'd also like thank both him and my KAPL manager Dr. Timothy Donovan for supporting me and helping me navigate inside the Naval Reactors culture.

In my two and a half years at MIT and in my four years at RPI previously, I have perhaps collectively learned more from my friends and my peers than from faculty, and I am forever indebted to them for their support, friendship, and knowledge. I'd especially like to thank the other collaborators on the DGM project, Dr. Lei Zhu and Matthew Everson. I owe a huge amount of gratitude to my officemate Jeremy Roberts, who has been an invaluable resource for me from my first day at MIT and who has never complained about my incessant interruptions while he does his own work. And, of course, I'd like to thank my closest friend in the nuclear industry, Bryan Herman, who I have followed from one university to another, from one internship to another, and will likely follow into the workforce.

Finally, I would like to thank my two loving parents. Before I reached the third grade, they declared that I was destined to be an engineer. They have given me more support and encouragement (and of course money!) than I can possibly thank them for. They have helped me achieve to the heights that I have risen, in both my education and the rest of my life.



# Contents

<b>Contents</b>	<b>7</b>
<b>List of Figures</b>	<b>10</b>
<b>List of Tables</b>	<b>12</b>
<b>1 Introduction</b>	<b>14</b>
1.1 Motivation and Objectives . . . . .	14
1.1.1 Motivation . . . . .	14
1.1.2 Objectives . . . . .	15
1.2 Multigroup Framework . . . . .	15
1.2.1 Multigroup Equations . . . . .	15
1.2.2 Multi-level Approach . . . . .	18
1.2.3 Self-shielding . . . . .	19
1.3 Ultrafine Energy Mesh . . . . .	23
1.3.1 Existing Uses . . . . .	23
1.3.2 Problems Associated with Use . . . . .	25
1.4 Discrete Basis Sets . . . . .	25
1.4.1 Discrete Legendre Polynomials . . . . .	27
1.4.2 Discrete Cosine Transforms . . . . .	28
1.4.3 Other Discrete Bases . . . . .	28

1.5	Discrete Generalized Multigroup Method . . . . .	30
1.5.1	Basic Idea . . . . .	30
1.5.2	Development . . . . .	30
1.5.3	Derivation . . . . .	32
1.5.4	Recondensation . . . . .	34
1.6	Fixed Point Iteration . . . . .	35
1.6.1	Picard Iteration . . . . .	35
1.6.2	Krasnoselskij Iteration . . . . .	36
1.6.3	Other Schemes . . . . .	37
1.7	Cross Sections Used in This Study . . . . .	38
1.7.1	SHEM361 . . . . .	38
1.7.2	NG2042 . . . . .	38
1.7.3	UF14767 . . . . .	39
1.7.4	Cross Section Generation . . . . .	39
<b>2</b>	<b>DGM Applied to Ultrafine Energy Mesh</b>	<b>41</b>
2.1	Validation of UF14767 Energy Mesh . . . . .	41
2.2	DGM Results . . . . .	43
2.2.1	Infinite Medium . . . . .	43
2.2.2	1-D Discrete Ordinates . . . . .	46
2.3	Complications and Concerns . . . . .	48
<b>3</b>	<b>Stability of DGM Procedure</b>	<b>50</b>
3.1	Simplest Example of Stability Issues . . . . .	50
3.1.1	Description . . . . .	50
3.1.2	Numerical Examples . . . . .	52
3.2	Improving Stability of Iteration Scheme . . . . .	55
3.2.1	Flux Updates . . . . .	55
3.2.2	Krasnoselskij Iteration . . . . .	55
3.2.3	Group Map . . . . .	60

<b>4 Computational Results</b>	<b>66</b>
4.1 BWR Core Benchmark . . . . .	66
4.1.1 Problem Description . . . . .	66
4.1.2 Results . . . . .	68
4.2 Ultrafine Pin-Cell Results . . . . .	73
<b>5 Conclusions and Future Work</b>	<b>76</b>
5.1 Conclusions . . . . .	76
5.2 Future Work . . . . .	78
5.2.1 Scattering Kernel Representation . . . . .	78
5.2.2 Lattice Physics Implementation . . . . .	78
<b>References</b>	<b>79</b>
<b>A TRESFIN Thermal Block</b>	<b>82</b>
<b>B SHEM Energy Mesh</b>	<b>85</b>
<b>C NJOY Inputs</b>	<b>88</b>
C.1 H-1 . . . . .	88
C.2 O-16 . . . . .	90
C.3 U-235 . . . . .	91
C.4 U-238 . . . . .	92

# List of Figures

1.1 Example of band in multiband formulation . . . . .	22
1.2 First few DLOPs with $N = 15$ . . . . .	29
1.3 First few DCTs with $N = 15$ . . . . .	29
1.4 Conceptual group mapping concept, $25 \rightarrow 4$ groups . . . . .	31
1.5 Continuous versus discrete bases for discrete data . . . . .	32
2.1 Comparison of UF14767 multigroup cross sections to inferred cross sections from Monte Carlo . . . . .	42
2.2 Geometry for simple slab 1-D pin-cell test problem . . . . .	46
3.1 Input versus output thermal to fast flux ratios for stable DGM case . . . . .	54
3.2 Input versus output thermal to fast flux ratios for unstable DGM case . . . . .	54
3.3 Input versus output thermal to fast flux ratios for DGM with flux update . . . . .	56
3.4 Instability in DGM recondensation procedure occurring in resonance group . . . . .	59
3.5 Eigenvalue versus iteration for modified Krasnoselskij procedure . . . . .	60
3.6 Total cross section for 10 group example problem . . . . .	62
3.7 Poor versus good choices of group map . . . . .	62
3.8 Poor choice of SHEM361 group map . . . . .	65
3.9 Good choice of SHEM361 group map . . . . .	65
4.1 Geometry of 1-D BWR benchmark problem . . . . .	67
4.2 Core 2 reaction rate errors, SHEM361 group structure . . . . .	69

4.3	Core 4 reaction rate errors, SHEM361 group structure . . . . .	69
4.4	Core 2 reaction rate errors, NG2042 group structure . . . . .	70
4.5	Core 4 reaction rate errors, NG2042 group structure . . . . .	70
4.6	Reaction rate errors, Core 2, $\lambda = 0.8$ , SHEM361 group structure . . . . .	72
4.7	Reaction rate errors, Core 4, $\lambda = 0.8$ , SHEM361 group structure . . . . .	72
4.8	Reaction rate errors, Core 2, $\lambda = 0.9$ , NG2042 group structure . . . . .	74
4.9	Reaction rate errors, Core 4, $\lambda = 0.9$ , NG2042 group structure . . . . .	74

# List of Tables

1.1	CEA 11,276-group energy mesh . . . . .	24
1.2	UF14767 energy mesh . . . . .	39
2.1	Comparison of eigenvalues: UF14767 multigroup vs. continuous energy cross sections .	41
2.2	Geometry specifications for Mosteller benchmark pin-cell . . . . .	44
2.3	Minor actinide concentrations used in test problems . . . . .	44
2.4	Number densities for test problems . . . . .	44
2.5	Example coarse-to-fine group mappings . . . . .	45
2.6	Convergence for UO <sub>2</sub> case, Mapping 1 . . . . .	45
2.7	Convergence for UO <sub>2</sub> case, Mapping 2 . . . . .	45
2.8	Convergence comparisons for MOX case, Mapping 1 . . . . .	46
2.9	Convergence comparisons for MOX case, Mapping 2 . . . . .	46
2.10	Isotopic concentrations of the materials in 1-D pin-cell . . . . .	47
2.11	1-D slab pin-cell DGM results . . . . .	47
2.12	Timing summary of recondensation steps for 1-D DGM problem . . . . .	48
3.1	Picard iterates for convergent 2 → 1 group infinite medium DGM procedure . . . . .	52
3.2	Picard iterates for non-convergent 2 → 1 group infinite medium DGM procedure . . . .	53
3.3	Picard iterates for 2 → 1 group infinite medium DGM procedure with flux update . . . .	56
3.4	Krasnoselskij iterates for 2 → 1 group infinite medium DGM procedure . . . . .	57
3.5	Iterations required for convergence of Krasnoselskij procedure . . . . .	57

3.6	Number densities used in SHEM361 infinite medium example problem . . . . .	58
3.7	$\lambda$ values for modified Krasnoselskij iteration procedures . . . . .	59
4.1	Isotopic compositions of materials in 1-D BWR benchmark problem . . . . .	67
4.2	Fine-to-coarse group maps for BWR benchmark calculations . . . . .	68
4.3	Timing results for benchmark problem with SHEM361 group structure . . . . .	71
4.4	Timing results for benchmark problem with NG2042 group structure . . . . .	73
4.5	UF14767 pin-cell problem results . . . . .	75
4.6	Timing summary of first few DGM iterations for pin-cell problem with UF14767 group structure . . . . .	75

# **Chapter 1**

## **Introduction**

### **1.1 Motivation and Objectives**

#### **1.1.1 Motivation**

Deterministic reactor physics methods are currently the industry standard for neutronics modeling and design of nuclear reactors. Deterministic calculations live in the multigroup energy discretization framework, and their accuracy is entirely dependent upon accurate multigroup cross section data.

For today's light water reactors, reactor physics is modeled with sufficient accuracy using a multi-level approach, where several levels of calculations are used. First, simplistic geometries are modeled with detailed energy dependence; next, several levels of increasing spatial complexity and decreasing energy resolution is performed. The success of this process is dependent upon energy spectrum effects being localized. In proposed reactor types, such as high temperature graphite moderated reactors and sodium cooled fast reactors, the neutron mean free path is much longer than in today's fleet of light water reactors. This causes the localized effects assumption to break down.

Also, as higher burnup fuel, mixed oxide fuel, and non-standard fuel cycles are considered, resonance self-shielding models employed today break down. Overlapping resonances, which are poorly handled by these models, become a common occurrence when several resonant isotopes are present in a fuel simultaneously. In today's light water reactors, plutonium-based mixed oxide fuels are already a reality. Actinide burning reactors, proposed to transmute the long-lived isotopes in nuclear waste, especially highlight this issue.

To address the challenges of future reactors, new self-shielding methodologies are needed. The optimal means of accounting for self-shielding is to use continuous energy nuclear data. Although this is easily accomplished in Monte Carlo simulations, these are too expensive to be used exclusively in

design and operational calculations. The most straightforward way to use continuous energy cross sections in a deterministic framework is to use the multigroup energy discretization with an ultrafine group structure. However, this is associated with a high degree of computational expense.

The Discrete Generalized Multigroup method could potentially reduce the computational cost associated with an ultrafine energy mesh. The method was developed at the Massachusetts Institute of Technology by Zhu and Forget [2010], and allows a fine energy structure to be represented by a coarse energy multigroup equation and higher order shape functions. This has been shown to provide an approximate fine group flux for a cost similar to that of the coarse group calculation. Using this method in conjunction with an ultrafine energy mesh could yield a flexible self-shielding methodology without a prohibitive computational expense.

### **1.1.2 Objectives**

The objectives of this thesis are to apply the Discrete Generalized Multigroup (DGM) method to an ultrafine energy mesh and to assess the feasibility of this procedure.

First, the DGM method is applied to simple geometries, including infinite media and 1-D slab geometries, using an ultrafine energy mesh. The goal of this work is to identify the obstacles to using DGM as a means to relax the need for self-shielding approximations. This analysis is presented in Ch. 2.

Once the obstacles are identified, algorithmic changes are presented to alleviate identified problems. The work performed and presented in this thesis focuses specifically on improving the stability of the procedure. This is accomplished by introducing Krasnoselskij fixed point iteration to the DGM framework and presenting a group mapping algorithm. This work is presented in Ch. 3.

Finally, using the improved recondensation procedure, computational results are presented in Ch. 4. Included are results with a 1-D BWR core benchmark problem for intermediate numbers of groups and simple 1-D results with the ultrafine energy mesh.

## **1.2 Multigroup Framework**

### **1.2.1 Multigroup Equations**

The workhorse of reactor physics calculations is the multigroup method [Duderstadt and Hamilton, 1976; Stacey, 2007; Hébert, 2009]. The energy dependence of the neutron transport equation is discretized into groups, inside which neutrons are assumed to be single-speed. Thus, the neutron flux and cross section data is assumed to be constant with respect to energy inside each group.

The alternative approach to using the multigroup method is to use a continuous representation of nuclear data. This is most commonly done with Monte Carlo methods, where individual neutron histories are modeled statistically and converge in aggregate to the neutron flux in the core. Although reactor design applications have begun to use Monte Carlo simulations in recent years, the computational expense required is still prohibitive for a full suite of design calculations. Thus, multigroup deterministic calculations are still a necessity for these applications.

Because of the very detailed shape in energy of neutron cross sections, a discretization in which cross sections are simply evaluated at discrete energy points would lead to aliasing and would not be representative of the true transport equation. Instead, the multigroup equations are based on the premise of conserving reaction rates and do so by the process of energy condensation.

The multigroup equations can be derived from the neutron transport equation. The time-independent integro-differential  $k$ -eigenvalue formulation will be used here. The transport equation is given as:

$$\begin{aligned} \hat{\Omega} \cdot \psi(\vec{r}, \hat{\Omega}, E) + \Sigma_t(\vec{r}, E) \psi(\vec{r}, \hat{\Omega}, E) \\ = \int_0^\infty dE' \int_{4\pi} d\hat{\Omega}' \Sigma_s(\vec{r}, E' \rightarrow E, \hat{\Omega}' \rightarrow \hat{\Omega}) \psi(\vec{r}, \hat{\Omega}', E') \\ + \frac{\chi(E)}{4\pi k} \int_0^\infty dE' \int_{4\pi} d\hat{\Omega}' \nu \Sigma_f(\vec{r}, E') \psi(\vec{r}, \hat{\Omega}', E'), \end{aligned} \quad (1.1)$$

where  $\hat{\Omega}$  is the direction of neutron travel;  $\vec{r}$  is the neutron position;  $E$  is the neutron energy;  $\Sigma_t$ ,  $\Sigma_s$ , and  $\nu \Sigma_f$  are the macroscopic total, scattering, and nu-fission cross sections, respectively;  $\chi$  is the output fission neutron energy spectrum; and  $\psi$  is the neutron angular flux. The scalar flux is given as:

$$\phi(\vec{r}, E) = \int_{4\pi} d\hat{\Omega} \psi(\vec{r}, \hat{\Omega}, E). \quad (1.2)$$

Although not required by the multigroup discretization, scattering will be assumed isotropic for simplicity in this presentation. With this assumption and the introduction of the scalar flux, the transport equation becomes:

$$\begin{aligned} \hat{\Omega} \cdot \psi(\vec{r}, \hat{\Omega}, E) + \Sigma_t(\vec{r}, E) \psi(\vec{r}, \hat{\Omega}, E) \\ = \frac{1}{4\pi} \int_0^\infty dE' \Sigma_s(\vec{r}, E' \rightarrow E) \phi(\vec{r}, E') + \frac{\chi(E)}{4\pi k} \int_0^\infty dE' \nu \Sigma_f(\vec{r}, E') \phi(\vec{r}, E'). \end{aligned} \quad (1.3)$$

Next, the transport equation is integrated in energy over group boundaries given as  $E \in [E_g, E_{g+1}]$ , and integrals then become sums of these groups:

$$\begin{aligned}
& \hat{\Omega} \cdot \int_{E_g}^{E_{g-1}} dE \psi(\vec{r}, \hat{\Omega}, E) + \int_{E_g}^{E_{g-1}} dE \Sigma_t(\vec{r}, E) \psi(\vec{r}, \hat{\Omega}, E) \\
&= \int_{E_g}^{E_{g-1}} dE \frac{1}{4\pi} \sum_{g'=1}^{N_g} \int_{E_{g'}}^{E_{g'-1}} dE' \Sigma_s(\vec{r}, E' \rightarrow E) \phi(\vec{r}, E') \\
&+ \int_{E_g}^{E_{g-1}} dE \frac{\chi(E)}{4\pi k} \sum_{g'=1}^{N_g} \int_{E_{g'}}^{E_{g'-1}} dE' \nu \Sigma_f(\vec{r}, E') \phi(\vec{r}, E').
\end{aligned} \tag{1.4}$$

The multigroup flux is then defined as:

$$\psi_g(\vec{r}, \hat{\Omega}) = \int_{E_g}^{E_{g-1}} dE \psi(\vec{r}, \hat{\Omega}, E) \tag{1.5}$$

$$\phi_g(\vec{r}) = \int_{E_g}^{E_{g-1}} dE \phi(\vec{r}, E). \tag{1.6}$$

Multigroup cross sections are defined as:

$$\Sigma_{t,g}(\vec{r}, \hat{\Omega}) = \frac{\int_{E_g}^{E_{g-1}} dE \Sigma_t(\vec{r}, E) \psi(\vec{r}, \hat{\Omega}, E)}{\int_{E_g}^{E_{g-1}} dE \psi(\vec{r}, \hat{\Omega}, E)} \tag{1.7}$$

$$\Sigma_{s,g' \rightarrow g}(\vec{r}) = \frac{\int_{E_{g'}}^{E_{g'-1}} dE' \int_{E_g}^{E_{g-1}} dE \Sigma_s(\vec{r}, E' \rightarrow E) \phi(\vec{r}, E')}{\int_{E_{g'}}^{E_{g'-1}} dE' \phi(\vec{r}, E')} \tag{1.8}$$

$$\nu \Sigma_{f,g}(\vec{r}) = \frac{\int_{E_g}^{E_{g-1}} dE \nu \Sigma_f(\vec{r}, E) \phi(\vec{r}, E)}{\int_{E_g}^{E_{g-1}} dE \phi(\vec{r}, E)} \tag{1.9}$$

$$\chi_g = \int_{E_g}^{E_{g-1}} dE \chi(E). \tag{1.10}$$

With these definitions, we arrive at the multigroup transport equation:

$$\begin{aligned}
& \hat{\Omega} \cdot \psi_g(\vec{r}, \hat{\Omega}) + \Sigma_{t,g}(\vec{r}, \hat{\Omega}) \psi_g(\vec{r}, \hat{\Omega}) \\
&= \frac{1}{4\pi} \sum_{g'=1}^G \Sigma_{s,g' \rightarrow g}(\vec{r}) \phi_{g'}(\vec{r}) + \frac{\chi_g}{4\pi k} \sum_{g'=1}^G \nu \Sigma_{f,g'}(\vec{r}) \phi_{g'}(\vec{r}).
\end{aligned} \tag{1.11}$$

In many applications, it is not convenient to have  $\Sigma_{t,g}$  depend on  $\hat{\Omega}$ . Thus, it is common to approximate  $\Sigma_{t,g}$  with:

$$\Sigma_{t,g}(\vec{r}) = \frac{\int_{E_g}^{E_{g-1}} dE \Sigma_t(\vec{r}, E) \phi(\vec{r}, E)}{\int_{E_g}^{E_{g-1}} dE \phi(\vec{r}, E)}. \quad (1.12)$$

With this approximation, the multigroup transport equation is slightly simplified to:

$$\begin{aligned} & \hat{\Omega} \cdot \psi_g(\vec{r}, \hat{\Omega}) + \Sigma_{t,g}(\vec{r}) \psi_g(\vec{r}, \hat{\Omega}) \\ &= \frac{1}{4\pi} \sum_{g'=1}^G \Sigma_{s,g' \rightarrow g}(\vec{r}) \phi_{g'}(\vec{r}) + \frac{\chi_g}{4\pi k} \sum_{g'=1}^G \nu \Sigma_{f,g'}(\vec{r}) \phi_{g'}(\vec{r}). \end{aligned} \quad (1.13)$$

## 1.2.2 Multi-level Approach

Although the multigroup energy discretization transforms the neutron transport equation of Eq. 1.3 into a much simpler and tractable equation in Eq. 1.11, the work is not done. The nuclear data used in Eq. 1.11 as defined in Eqs. 1.7-1.10 depends upon the neutron flux—the very thing we seek to solve with the transport equation. This issue is best explained by the NJOY manual [Macfarlane, 2000]:

*“Wait a minute,” you ask, “the purpose of solving the transport equation is to get the flux, but I have to know the flux to compute the multigroup constants!” This conundrum is the source of much of the “art” in using multigroup methods.*

In practice, this is addressed through the use of a multi-level approach [Hébert, 2009]. Rather than modeling the neutronic behavior of a nuclear reactor with a single calculation, several calculations feed into each other at varying energy and spatial scales.

At the first level, evaluated nuclear data is processed into group cross sections. This is done using the NJOY nuclear data processing system [Macfarlane, 2000]. From evaluated nuclear data files, resonances are reconstructed to produce a point-wise cross section.

Next, a self-shielding step is performed. Section 1.2.3 explains some of the current methodologies for this in more detail. In some cases, this step is performed with NJOY’s groupr module, using an assumed flux shape. Fine group cross sections ( $\mathcal{O}(50 - 400)$  groups) are then generated as a function of background. Alternatively, hyper-fine group cross sections ( $\mathcal{O}(1000 - 10000)$  groups) can be generated and used in a very simple spatial calculation, usually a pin-cell or an infinite medium. This calculation is used to produce the fine group cross section set.

At the next level, lattice calculations are performed with  $\mathcal{O}(50 - 400)$  groups. The spatial complexity is increased to model a single assembly in the reactor with reflective boundary conditions. These calculations are generally performed with transport theory with detailed spatial and angular representation, using the method of characteristics, the collision probability method, or the discrete ordinates method.

Lattice calculations are used to generate a reactor database, including broad-group cross sections ( $\mathcal{O}(2 - 20)$  groups) as a function of temperature and burn-up.

Finally, the full core calculation is performed. This increases the spatial scale to that of the full reactor, but the angular and spatial detail is decreased to homogenized regions. The industry standard for these calculations is nodal diffusion theory.

Although this approach has been very successful in the modeling of classical light water reactors (LWRs), each energy condensation step introduces errors arising from the approximations involved. As novel reactor types are suggested and complexities are added to existing reactors, the cross section energy condensation process is showing its limitations. For instance, the reflective boundary conditions used at the lattice level assume that there is not much interaction between lattices. While this is a somewhat reasonable assumption in current LWRs, this assumption breaks down in fast reactors or graphite moderated reactors, which have much longer mean free paths, and where strong heterogeneities—such as MOX assemblies neighboring UO<sub>2</sub> assemblies—are present.

### 1.2.3 Self-shielding

Perhaps the most important aspect of the energy condensation process is to account for self-shielding effects. Because of the very large absorption cross section associated with resonances, the energy-dependent neutron flux has large depressions at these resonances. These flux depressions lower the reaction rate compared to what would be expected if the flux was not sensitive to the resonances.

There is also a spatial component to self-shielding. At the interface between a resonant material and a moderator, the flux in the resonant material is heavily influenced by neutrons streaming in from the moderator. Deep within a region with a lumped resonant material, the spectrum would be expected to be very different.

### Bondarenko Methods

The classical means of treating resonance self-shielding is via *Bondarenko* or *equivalence in dilution* methods.

In an infinite medium, the size of the flux depression near a resonance is a function not only of the shape of the resonance but also of the amount of non-resonant interactions occurring. Consider an infinite medium comprised exclusively of U-238. A neutron in this medium near a resonance would be almost assuredly absorbed. Thus, a very large flux depression near the resonance is expected. Now, consider an infinite medium comprised of nearly all water with a dilute amount of U-238 present. Although many more absorptions in U-238 would be expected near the resonance than away from

it, most neutrons would interact with water and not with the U-238. Thus, the flux shape would be insensitive to the resonance structure of U-238. Of course, in practice, we expect to observe intermediate ranges of these scenarios. This is the concept of *dilution*.

This concept is represented quantitatively by the introduction of the dilution cross section:

$$\sigma_d = \frac{\Sigma^+}{N^*}, \quad (1.14)$$

where  $\Sigma^+$  represents the macroscopic cross section of the non-resonant isotopes near the resonance and  $N^*$  is the number density of the resonant isotope. Here and in subsequent equations, the superscript + references the non-resonant isotopes; the superscript \* references the resonant isotope. Non-resonant cross sections are assumed to be nearly constant near the resonance.

The flux  $\phi$  is then factored as a product of an asymptotic spectrum  $\psi$  and a fine structure function  $\varphi$ :

$$\phi(E) = \psi(E)\varphi(E), \quad (1.15)$$

where the asymptotic spectrum is the shape of the flux assuming there are no effects from the resonance and the fine structure function accounts for the detailed shape caused by the resonance.

With this idea, approximations can be made by considering the width of the resonance compared to the average energy loss per collision in the medium. The two extremes are the narrow resonance (NR) model and the wide resonance (WR) model, sometimes also referred to as the narrow resonance infinite mass (NRIM) model [Duderstadt and Hamilton, 1976; Reuss, 2008].

The NR model assumes neutrons have large changes in energy with respect to the width of resonances following scattering collisions. This is best applied for high energy resonances in a mixed medium. The fine structure function is given by:

$$\varphi_{NR}(E) = \frac{\sigma_p^* + \sigma_d}{\sigma_t^*(E) + \sigma_d}, \quad (1.16)$$

where  $\sigma_p^*$  is the potential scattering cross section of the resonant isotope.

The WR model assumes the opposite, that neutrons have small changes in energy with respect to the width of the resonance. This is best applied to low-lying resonances in a lumped fuel. The fine structure function is given by:

$$\varphi_{WR} = \frac{\sigma_d}{\sigma_t^*(E) - \sigma_s^*(E) + \sigma_d}. \quad (1.17)$$

In practice, most resonances lie somewhere between these two cases. One means of addressing this is via the intermediate resonance (IR) model [Bell and Glasstone, 1970]. Here, the flux is linearly interpolated between the two extreme approximations with constant  $\lambda$ . The fine structure function is given by:

$$\varphi_{IR} = \frac{\lambda \sigma_p^* + \sigma_d}{\sigma_t^*(E) - (1-\lambda)\sigma_s^*(E) + \sigma_d}. \quad (1.18)$$

All of these models assume a single resonant isotope. In order to model a medium with multiple resonant isotopes, one must consider each isotope individually, assuming the cross section of each other resonance is constant. The process is iterated on until the dilution cross section for each isotope is converged. However, this process breaks down for overlapping resonances. With overlapping resonances, assuming one isotope's cross section is constant near another isotope's resonance is no longer valid.

In a heterogeneous medium, spatial effects must be considered. These are addressed by equivalence theory, where the system is represented by an infinite medium in which reaction rates are representative of the heterogeneous system. This is accomplished by adding an escape cross section  $\sigma_e$  to the dilution cross section  $\sigma_d$ .

The simplest approach is via the Bell-Wigner approximation [Reuss, 2008]. Bell and Wigner fit collision probabilities to simple functions and approximate  $\sigma_e$  with:

$$\sigma_e = \frac{b}{lN^*}, \quad (1.19)$$

where  $b$  is the Bell factor, a tabulated parameter characterizing the geometry, and  $l$  is the mean chord length, given by:

$$l = \frac{4V_f}{S_f}, \quad (1.20)$$

or four times the inverse of the surface to volume ratio for any convex body of lumped resonant material.

In an LWR, the collision probabilities can be adjusted for additional accuracy by considering the probability that a neutron from one fuel pin may travel to another fuel pin and be absorbed. This is represented by modifying the Bell factor by a Dancoff factor  $C$ . The Bell factor becomes:

$$b = \frac{(1-C)b_0}{1-C+Cb_0}, \quad (1.21)$$

where  $b_0$  is the Bell factor computed without the Dancoff factor.

## Subgroup Methods

Another class of self-shielding methods are *subgroup* or *multiband* methods [Cullen, 2010].

In this approach, the fine structure of the cross section inside a desired energy group is split into several bands, based on the value of the cross section. For instance, Fig. 1.1 shows an example cross section and band. Here, the band includes cross sections on the flanks of a large resonance and at the peak of a smaller resonance.

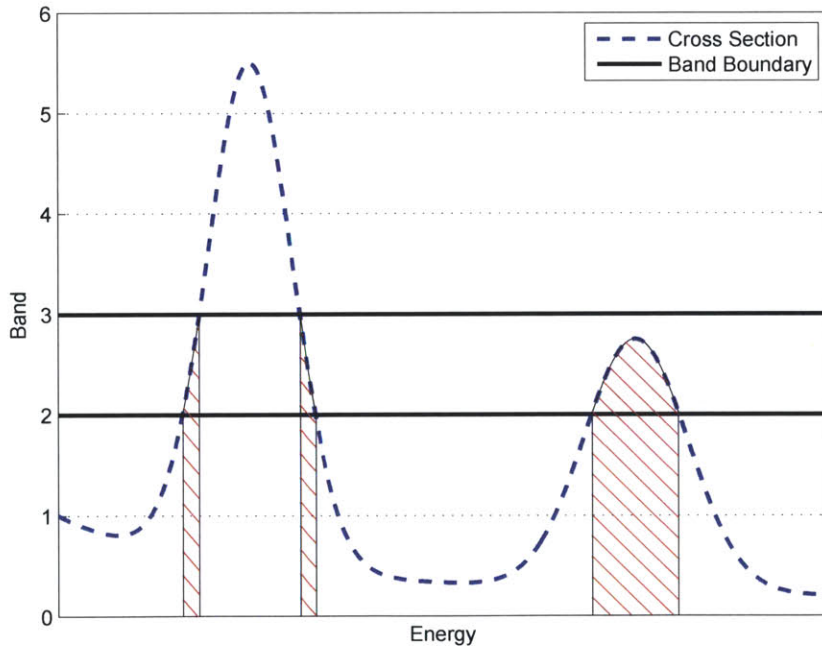


Figure 1.1: Example of band in multiband formulation. Probability of selecting cross section in this band is proportional to the area under the curve.

This allows the Riemann integrals over energy for resonant quantities to be replaced by Lebesgue integrals over total cross section. These integrations are performed with quadratures known as probability tables, which give the ratio of the area bounded by the cross section within a band to the area of the cross section within the full energy group.

Subgroup methods are the standard approach for the unresolved resonance range. Although they have been applied to the resolved resonance range, the underlying approximation that the scattering

resonances are not correlated with the absorption resonances makes them not the preferred method for resolved resonance self-shielding [Hébert, 2009].

## 1.3 Ultrafine Energy Mesh

In order to circumvent approximations used with self-shielding models, continuous or near-continuous energy data can be used [Cullen, 2010]. In the deterministic framework, this generally involves using an ultrafine group structure, containing several thousands of energy groups. By finely discretizing the resonance structure, the approximation that the nuclear data and the neutron flux are flat with respect to energy inside a group is valid.

### 1.3.1 Existing Uses

Numerous examples of existing uses of an ultrafine energy mesh can be noted in current applications.

#### CENTRM

The CENTRM code as part of the SCALE package developed at the Oak Ridge National Laboratory performs self-shielding calculations with point-wise data [Williams and Asgari, 1995]. CENTRM uses a standard multigroup treatment above and below the resonance range, and a point-wise treatment with 30,000-70,000 points to resolve the resonances of important isotopes. A submoment expansion is used to treat the scattering kernel to reduce the inefficiency of computing scattering sources for such a fine energy structure. To account for spatial self-shielding, CENTRM solves pin-cell calculations in a 1-D cylindrical discrete ordinates framework. This geometry requires a white boundary condition be used, which is generally considered to be a poor representation of a physical system. A 2-D pin-cell version, known as GEMINI, was developed but was found to be very slow.

#### RAZOR

The RAZOR code by Zerkle et al. [1997] employed at Bettis Laboratory uses near-continuous data to generate broad group cross sections for diffusion theory calculations. Because of the very fine energy structure, in-group scattering is assumed to be negligible and is pushed to the first down-scatter group, leading to purely absorbing equations to be solved. The scattering kernel is split into an inelastic portion represented with a coarse group structure and an elastic portion, which is computed on the fly with simple kinematics. The solution algorithm uses a dual energy resolution, such that the fine structure of the scattering sources is modeled for an energy range near the source and only a coarse energy dependence is used otherwise.

## AEGIS

Another use of an ultrafine group library is in the Japanese code AEGIS [Sugimura and Yamamoto, 2007; Yamamoto et al., 2010]. A 32,000-group ultrafine library is used for resonance treatment, with the energy structure being chosen via a sensitivity analysis. Calculations with this energy mesh are slowing down calculations in the resolved resonance region. Inelastic scattering is ignored and scattering is assumed to be isotropic in the center of mass. Also, due to the large expense in computing the scattering source directly, a  $1/E$  shape is assumed throughout the resonance region.

## APOLLO

The French code APOLLO developed by CEA uses an 11,276-group ultrafine library [Aggery, 1999]. The energy mesh uses a 524-group thermal block dubbed TRESFIN, given in Appendix A. Above thermal energies, equal lethargy bins are used inside broad energy bands. A summary of the group structure is given in Tab. 1.1.

## PARAGON

Westinghouse developed a 6,064-group library for use with the lattice physics code PARAGON [Huria and Ouisloumen, 2008]. The energy mesh started with the SHEM group structure [Hfaiedh and Santamarina, 2005] below 23 eV and constant lethargy intervals in the resonance range. Comparing to reaction rate tallies from MCNP5, the group boundaries were optimized to minimize deviation inside each energy mesh. The resulting cross-section library was used in a 2-D full core PWR calculation, and results agreed with MCNP within 80 pcm [Kucukboyaci et al., 2009]. Westinghouse also developed a 30,069 group mesh for comparison and determined that no additional benefit was gained over the optimized 6,064 group structure.

Table 1.1: CEA 11,276-group energy mesh

Energy Range	Mesh Structure
$E \leq 5.04348\text{eV}$	TRESFIN
$5.04348 < E \leq 51\text{eV}$	$\Delta u = 1/480$
$51 < E \leq 203\text{eV}$	$\Delta u = 1/960$
$203 < E \leq 1434\text{eV}$	$\Delta u = 1/1920$
$1434\text{eV} < E \leq 19.64\text{MeV}$	$\Delta u = 1/480$

### 1.3.2 Problems Associated with Use

The main problem associated with ultrafine energy meshes is the large computational expense associated with them. By discretizing the energy structure so finely, the size of the multigroup problem increases significantly.

Although all aspects of the problem increase in complexity, the scattering source scales most poorly with the number of groups. An explicit representation of the scattering matrix requires an extraordinary amount of memory. For instance, with 15,000 groups, a single scattering matrix for a material containing hydrogen requires approximately 1 GB of memory to store in double precision. When this is multiplied by a desired number of materials and a desired number of Legendre moments, the memory footprint requires significant computational resources. Also, such large scattering matrices are very expensive in terms of floating point operations when computing scattering sources.

Self-shielding methodologies have employed these structures with modest success for very simplified geometries in slowing down problems. However, large scale design calculations cannot be performed at this degree of expense outside of benchmarking.

## 1.4 Discrete Basis Sets

A basis is a set of linearly independent functions that can be combined to represent a general function inside some functional space. For a given set of basis functions  $\{\zeta_i\}$  and a function  $f$  that lies within their span, there exists a set of coefficients  $\{c_i\}$  such that:

$$f = \sum_i c_i \zeta_i. \quad (1.22)$$

In order to fully represent a general function in  $\mathcal{R}^n$ , an infinite number of independent  $n$ -dimensional basis functions are needed.

For many common applications of a basis set, orthogonality is desired. The orthogonality condition is given as:

$$\int \zeta_i \zeta_j d\vec{\omega} = \frac{\delta_{ij}}{a_i}, \quad (1.23)$$

where  $\delta_{ij}$  is the Kronecker delta function,  $a_i$  is some constant and a property of the given basis, and  $\vec{\omega}$  represents any independent variables in the space. Here, a unity weight is assumed. Orthogonality

conditions can be defined with the inclusion of a non-unity weight function, but bases derived from this definition are not used in this thesis.

The coefficients  $\{c_i\}$  for an orthogonal expansion can be found by multiplying Eq. 1.22 by one of the basis functions, integrating, and applying the orthogonality condition:

$$\int f \zeta_j d\vec{\omega} = \int \sum_i c_i \zeta_i \zeta_j d\vec{\omega} = c_j \int \zeta_j \zeta_j d\vec{\omega} = \frac{c_j}{a_j} \quad (1.24)$$

$$c_j = a_j \int f \zeta_j d\vec{\omega}. \quad (1.25)$$

Moments of the function  $f$  are then defined as:

$$f_i = \int f \zeta_i d\vec{\omega}, \quad (1.26)$$

and Eq. 1.22 becomes:

$$f = \sum_i a_i f_i \zeta_i. \quad (1.27)$$

When representing discrete functions, where the independent variable is only allowed to assume discrete values, a discrete basis is a natural fit. A discrete function  $g$ , given as a function of a single independent variable that can take on  $N + 1$  discrete values indexed by  $K$ , can be represented by a basis set  $\{\xi_i^N\}$ :

$$g(K) = \sum_{i=0}^N c_i \xi_i^N(K). \quad (1.28)$$

For a discrete space with  $N + 1$  discrete values, a general function can be exactly represented by a linear combination of  $N + 1$  independent basis functions.

The orthogonality condition with unity weight for a discrete basis becomes:

$$\sum_{K=0}^N \xi_i^N(K) \xi_j^N(K) = \frac{\delta_{ij}}{a_i}. \quad (1.29)$$

Analogous to the continuous expansions, moments of the function  $g$  are defined as:

$$g_i = \sum_{K=0}^N g(K) \xi_i^N(K), \quad (1.30)$$

and Eq. 1.28 becomes:

$$g = \sum_{i=0}^N a_i g_i \xi_i^N(K). \quad (1.31)$$

#### 1.4.1 Discrete Legendre Polynomials

Discrete Legendre orthogonal polynomials (DLOPs) [Neuman and Schonbach, 1974] are a set of basis functions similar to the familiar continuous shifted Legendre polynomials. DLOPs are held to the orthogonality condition of Eq. 1.29. DLOPs are polynomial functions of  $K$ . As orthogonal polynomials, the DLOPs are fully defined by a normalization condition:

$$\xi_m^N(0) = 1, \quad \forall m. \quad (1.32)$$

The normalization factor is given by:

$$a_m = (2m+1) \frac{N^{(m)}}{(N+m+1)^{(m+1)}}, \quad (1.33)$$

where  $N^{(m)}$  is the  $m^{\text{th}}$  fading factorial of  $N$  and is defined as:

$$N^{(m)} = \begin{cases} N(N-1)(N-2)\dots(N-m-1), & m > 0 \\ 1, & m = 0. \end{cases} \quad (1.34)$$

The first two DLOPs are:

$$\xi_0^N(K) = 1 \quad (1.35)$$

$$\xi_1^N(K) = (N - 2K)/N. \quad (1.36)$$

With these, a recurrence relation can be used to generate higher order DLOPs:

$$(m+1)(N-m)\xi_{m+1}^N(K) = (2m+1)(N-2K)\xi_m^N(K) - m(N+m+1)\xi_{m-1}^N(K). \quad (1.37)$$

A particularly important property of DLOPs can be derived using Eqs. 1.29 and 1.35:

$$\sum_{K=0}^N \xi_l^N(K) = \frac{\delta_{0l}}{a_0} = \begin{cases} N+1, & l=0 \\ 0 & l \neq 0. \end{cases} \quad (1.38)$$

A plot of the first few DLOPs with  $N = 15$  is given in Fig. 1.2. Dotted lines connect the discrete values. This is to aid in visualization; it does not imply a continuous definition of the basis.

### 1.4.2 Discrete Cosine Transforms

Another possible discrete basis is the discrete cosine transform (DCT) [Ahmed et al., 1974]. The Type II transform is presented here. The DCT basis is given by:

$$\xi_m^N(K) = \cos\left(\frac{m\pi}{N+1}(K + 1/2)\right). \quad (1.39)$$

The DCT basis is orthogonal and follows the requirement of Eq. 1.29. The normalization coefficients are given by:

$$a_m = \begin{cases} \frac{1}{N+1}, & m=0 \\ \frac{2}{N+1}, & m \neq 0. \end{cases} \quad (1.40)$$

Because the DCTs can be generated directly with Eq. 1.39, no recursion relation is needed. This is beneficial numerically, as recursion relations lead to accumulation of roundoff error and loss of orthogonality for high order polynomials.

The first few DCTs with  $N = 15$  are plotted in Fig. 1.3. As in Fig. 1.2, dotted lines connect the discrete values. This is to aid in visualization; it does not imply a continuous definition of the basis.

### 1.4.3 Other Discrete Bases

Many other discrete bases exist and are feasible to use in the context of this thesis, but were not included in the scope of this study.

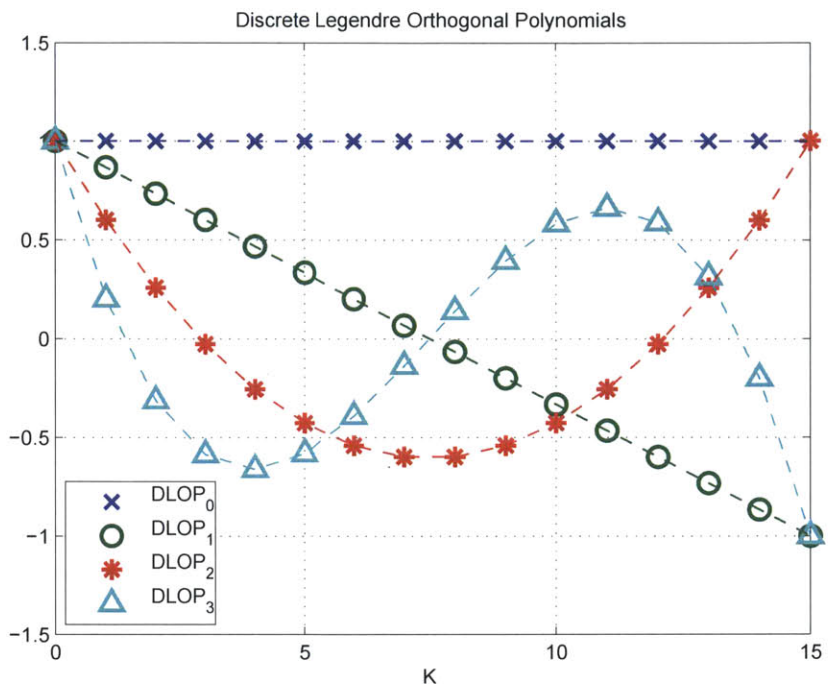


Figure 1.2: First few DLOPs with  $N = 15$

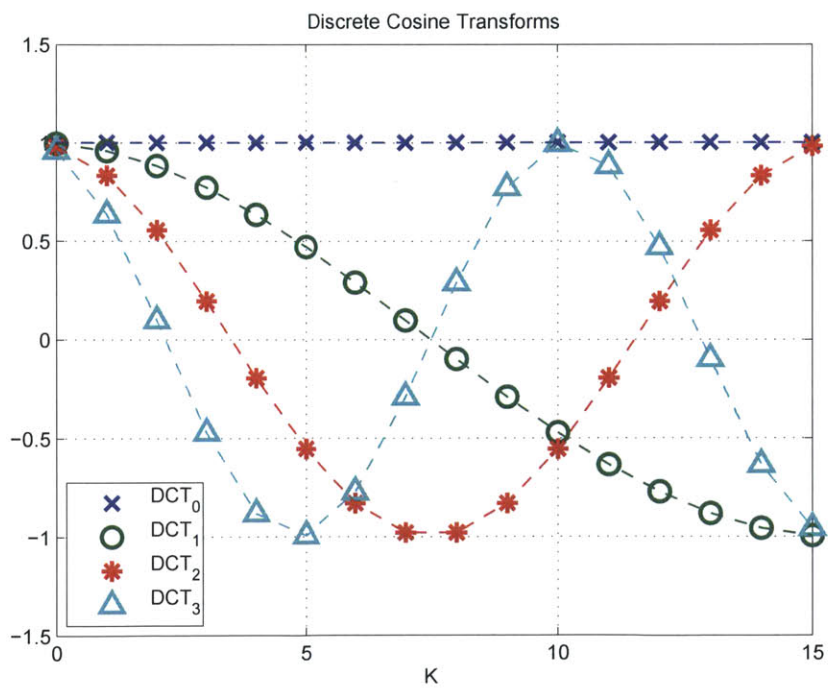


Figure 1.3: First few DCTs with  $N = 15$

In past work by Zhu [2012], discrete Tchebyshev polynomials (DTs) were used with the DGM framework used in this thesis. There, DTs were shown to be less sensitive to accumulation of roundoff error and loss of orthogonality than the DLOPs, but still exhibited this behavior for very high order polynomials.

A feasibility study on using an adaptive energy mesh by van Rooijen [2012] used discrete wavelet transforms (DWTs) to treat the energy variable. However, the DWTs have not been applied in the DGM framework.

## 1.5 Discrete Generalized Multigroup Method

### 1.5.1 Basic Idea

The Discrete Generalized Multigroup (DGM) method expands the energy dependence of the multigroup neutron transport equations with a discrete basis set. A fine group structure is mapped to a coarse group structure, where each coarse group contains some number of fine groups. Fig. 1.4 shows a conceptual  $25 \rightarrow 4$  group map.

The energy dependence of the fine group can be fully represented with the coarse group and a  $N_G - 1$  order expansion, if  $N_G$  fine groups are in a coarse group.

The zeroth order equations are identical to the coarse group multigroup equations with cross sections condensed in the standard multigroup framework. The higher order equations provide shape information for the energy spectrum inside the coarse groups.

As shown in Sec. 1.5.3, the higher order solutions are very simple equations—purely absorbing, decoupled, fixed sourced equations. The computational expense associated with the solution of these is negligible. Thus, the total computational expense associated with solving the DGM equations is approximately the same as the coarse group equations.

A recondensation procedure is introduced in Sec. 1.5.4. Here, the coarse group cross sections can be improved by solving the DGM equations multiple times.

### 1.5.2 Development

An energy spectral unfolding method was first proposed by Forget and Rahnema [2007] and was developed into the generalized energy condensation theory by Rahnema et al. [2008]. In this work, the standard energy condensation procedure was generalized by assuming the energy dependence of the neutron flux could be expanded with an orthogonal basis set. The zeroth order moment equation

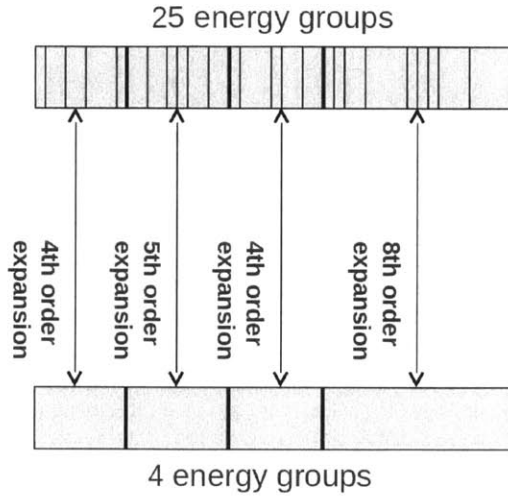


Figure 1.4: Conceptual group mapping concept,  $25 \rightarrow 4$  groups

is identical to the familiar coarse multigroup equations. However, higher order moment equations were introduced that provide information to unfold the fine energy structure of the flux. This work primarily used continuous shifted Legendre polynomials as the basis.

It was found that continuous basis functions were not well suited for representing multigroup fluxes. In order to represent the discrete data, continuous polynomials require very high order expansions and knowledge of the location of the step boundaries. Near the discontinuities, Gibbs phenomena is observed; that is, large unphysical oscillations are observed. Also, the strong possibility of negative values in the representation can wreak havoc on reactor physics calculations.

A discrete basis fits the multigroup framework much more naturally. The fine structure can be exactly represented with an amount of moments equal to the number of discrete values. This alleviates the issues of truncation error and the high computational expense associated with very large order expansions. Fig. 1.5 shows this behavior for a simple example.

Zhu and Forget [2010] introduced discrete bases to the generalized multigroup framework. The method was then dubbed the “Discrete Generalized Multigroup” or DGM method. Recognizing the quality of the fine structure of the solution was directly related to the quality of the guessed spectrum used in collapsing the cross sections, a recondensation procedure was introduced [Zhu and Forget, 2011a]. Here, the unfolded spectrum was used as the guessed spectrum for a subsequent calculation. This procedure could be iterated on until desired accuracy is achieved. Under certain conditions, this procedure is fully consistent with a direct solution of the fine group problem.

Further development of DGM is ongoing at the Massachusetts Institute of Technology. Selected publications include Zhu and Forget [2011b]; Gibson and Forget [2012a,b]. Parallel work has also

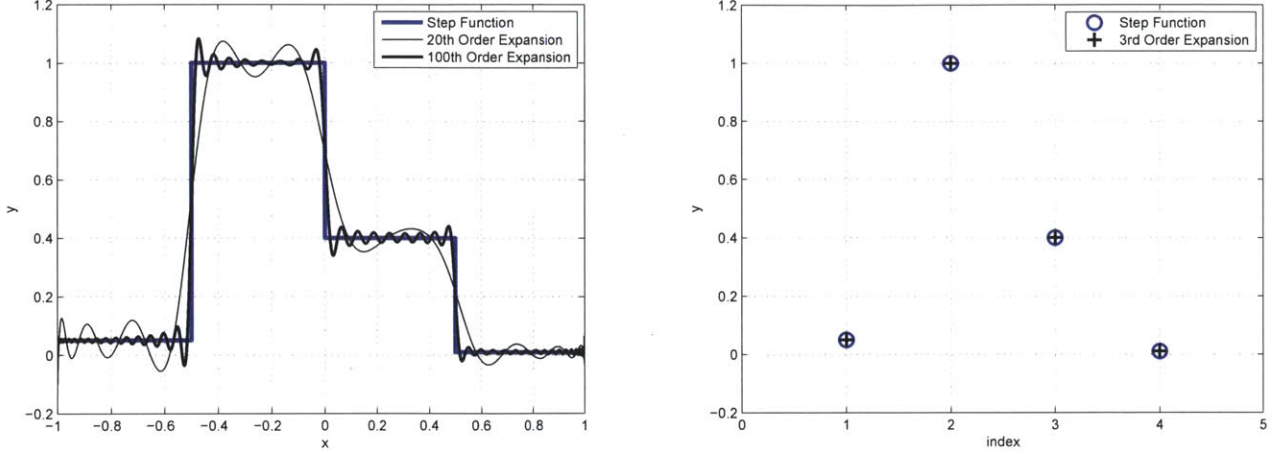


Figure 1.5: Continuous basis functions (left) compared to discrete basis functions (right) for discrete data

continued at Georgia Institute of Technology, with selected publications including Douglass and Rahnema [2011, 2012a,b].

### 1.5.3 Derivation

First, consider the multigroup transport equation of Eq. 1.13.

$$\begin{aligned} \hat{\Omega} \cdot \psi_g(\vec{r}, \hat{\Omega}) + \Sigma_{t,g}(\vec{r})\psi_g(\vec{r}, \hat{\Omega}) \\ = \frac{1}{4\pi} \sum_{g'=1}^{N_g} \Sigma_{s,g' \rightarrow g}(\vec{r})\phi_{g'}(\vec{r}) + \frac{\chi_g}{4\pi k} \sum_{g'=1}^{N_g} \nu \Sigma_{f,g'}(\vec{r})\phi_{g'}(\vec{r}). \end{aligned} \quad (1.41)$$

As in the presentation of the multigroup equations in Sec. 1.2.1, isotropic scattering is assumed for simplicity but is not a requirement of this derivation. Likewise, the  $k$ -eigenvalue formulation is presented, but can easily be extended to time dependent problems. The fine group total cross section is assumed to be well represented by Eq. 1.12 and not a function of  $\hat{\Omega}$ .

Next, the energy groups are divided into coarse groups. Each fine group  $g$  is assumed to be contained inside some coarse group  $G$ :

$$\begin{aligned} \hat{\Omega} \cdot \psi_g(\vec{r}, \hat{\Omega}) + \Sigma_{t,g}(\vec{r})\psi_g(\vec{r}, \hat{\Omega}) \\ = \frac{1}{4\pi} \sum_{G'=1}^{N_G} \sum_{g' \in G'} \Sigma_{s,g' \rightarrow g}(\vec{r})\phi_{g'}(\vec{r}) + \frac{\chi_g}{4\pi k} \sum_{G'=1}^N \sum_{g' \in G'} \nu \Sigma_{f,g'}(\vec{r})\phi_{g'}(\vec{r}). \end{aligned} \quad (1.42)$$

Shifted discrete basis functions  $\xi_i^G$  are introduced. These are equivalent to the previously presented basis functions except that the domain of the index ranges from the minimum to the maximum fine

group index rather than  $0 \dots N$ . The superscript  $G$  indicates the coarse group, indicating both the minimum fine group index and the number of fine groups in that coarse group. For a coarse group  $G$  containing  $N_G$  fine groups  $g_1 \dots g_{N_G}$ , that is:

$$\hat{\xi}_i^G(g) \equiv \xi_i^{N_G-1}(g - g_1). \quad (1.43)$$

Each term is multiplied by the shifted discrete basis function and summed over the fine groups in the coarse group:

$$\begin{aligned} \hat{\Omega} \cdot \sum_{g \in G} \hat{\xi}_i^G(g) \psi_g(\vec{r}, \hat{\Omega}) + \sum_{g \in G} \hat{\xi}_i^G(g) \Sigma_{t,g}(\vec{r}) \psi_g(\vec{r}, \hat{\Omega}) \\ = \sum_{g \in G} \hat{\xi}_i^G(g) \frac{1}{4\pi} \sum_{G'=1}^N \sum_{g' \in G'} \Sigma_{s,g' \rightarrow g}(\vec{r}) \phi_{g'}(\vec{r}) \\ + \sum_{g \in G} \hat{\xi}_i^G(g) \frac{\chi_g}{4\pi k} \sum_{G'=1}^N \sum_{g' \in G'} v \Sigma_{f,g'}(\vec{r}) \phi_{g'}(\vec{r}). \end{aligned} \quad (1.44)$$

Flux moments are then defined as:

$$\psi_{i,G}(\vec{r}, \hat{\Omega}) = \sum_{g \in G} \hat{\xi}_i^G(g) \psi_g(\vec{r}, \hat{\Omega}) \quad (1.45)$$

$$\phi_{i,G}(\vec{r}) = \sum_{g \in G} \hat{\xi}_i^G(g) \phi_g(\vec{r}). \quad (1.46)$$

DGM cross sections are defined as:

$$\Sigma_{t,0,G}(\vec{r}) = \frac{\sum_{g \in G} \hat{\xi}_0^G(g) \Sigma_{t,g}(\vec{r}) \phi_g(\vec{r})}{\sum_{g \in G} \hat{\xi}_0^G(g) \phi_g(\vec{r})} = \frac{\sum_{g \in G} \Sigma_{t,g}(\vec{r}) \phi_g(\vec{r})}{\sum_{g \in G} \phi_g(\vec{r})} \quad (1.47)$$

$$\delta_{i,G}(\vec{r}, \hat{\Omega}) = \frac{\sum_{g \in G} \hat{\xi}_i^G(g) (\Sigma_{t,g}(\vec{r}) - \Sigma_{t,0,g}(\vec{r})) \psi_g(\vec{r}, \hat{\Omega})}{\sum_{g \in G} \psi_g(\vec{r}, \hat{\Omega})} \quad (1.48)$$

$$\Sigma_{s,i,G' \rightarrow G}(\vec{r}) = \frac{\sum_{g \in G} \hat{\xi}_i^G(g) \sum_{g' \in G'} \Sigma_{s,g' \rightarrow g}(\vec{r}) \phi_g(\vec{r})}{\sum_{g \in G} \phi_g(\vec{r})} \quad (1.49)$$

$$v \Sigma_{f,G}(\vec{r}) = \frac{\sum_{g \in G} \hat{\xi}_i^G(g) v \Sigma_{f,g}(\vec{r}) \phi_g(\vec{r})}{\sum_{g \in G} \phi_g(\vec{r})} \quad (1.50)$$

$$\chi_{i,G} = \sum_{g \in G} \hat{\xi}_i^G(g) \chi_g. \quad (1.51)$$

In the definition of the DGM cross sections, the total cross section is split into two terms,  $\Sigma_{t,0,G}$  and  $\delta_{i,G}$ .  $\Sigma_{t,0,g}$  is defined as an analog of the approximation in Eq. 1.12, and  $\delta_{i,G}$  is a correction term to retain the angular dependence. This formulation enhances stability, as it avoids putting higher order flux moments—which may be arbitrarily small—in the denominator.

The DGM equations are then:

$$\begin{aligned} \hat{\Omega} \cdot \psi_{i,G}(\vec{r}, \hat{\Omega}) + \Sigma_{t,0,G}(\vec{r})\psi_{i,G}(\vec{r}, \hat{\Omega}) + \delta_{i,G}(\vec{r}, \hat{\Omega})\psi_{0,G}(\vec{r}, \hat{\Omega}) \\ = \frac{1}{4\pi} \sum_{G'=1}^N \Sigma_{s,i,G' \rightarrow G}(\vec{r})\phi_{0,G'}(\vec{r}) + \frac{\chi_{i,g}}{4\pi k} \sum_{G'=1}^N \nu \Sigma_{f,G'}(\vec{r})\phi_{0,G'}(\vec{r}). \end{aligned} \quad (1.52)$$

The zeroth order, or  $i = 0$ , DGM equation is entirely equivalent to the coarse group multigroup problem in Eq. 1.11 with cross sections collapsed by the standard procedure. The sum of  $\Sigma_{t,0,G}$  and  $\delta_{0,G}$  is the total cross section defined in Eq. 1.7. The higher order,  $i > 0$ , equations are purely absorbing fixed source equations, the solution to which give shape information regarding the fine group flux. Because the right hand side of the higher order equations do not depend upon their own solutions, they are not eigenproblems. This is most easily seen by recasting the equations in operator notation:

$$\begin{aligned} \mathbb{T}_0 \Psi_0 &= \mathbb{S}_0 \Phi_0 + \frac{1}{k} \mathbb{F}_0 \Phi_0 & i = 0 \\ \mathbb{T}_i \Psi_i &= \mathbb{S}_i \Phi_0 + \frac{1}{k} \mathbb{F}_i \Phi_0 & i > 0, \end{aligned} \quad (1.53)$$

where  $\mathbb{T}$  is the streaming and collision transport operator,  $\mathbb{S}$  is the scattering matrix,  $\mathbb{F}$  is the fission matrix, and  $\Psi$  and  $\Phi$  are the angular and scalar flux vectors.

After solving these equations, the fine group flux can be unfolded from the flux moments:

$$\psi_g(\vec{r}, \hat{\Omega}) = \sum_{i=0}^{N_G-1} a_i \hat{\xi}_i^G(g) \psi_{i,G}(\vec{r}, \hat{\Omega}) \quad (1.54)$$

$$\phi_g(\vec{r}) = \sum_{i=0}^{N_G-1} a_i \hat{\xi}_i^G(g) \phi_{i,G}(\vec{r}). \quad (1.55)$$

This unfolded flux is an approximation of the fine group flux. However, it is limited in accuracy by the choice of the guessed flux used to weight the DGM cross sections from Eqs. 1.47-1.51.

#### 1.5.4 Recondensation

Recognizing that the unfolded flux is a better approximation to the true solution than the initial guessed flux, an intuitive procedure is to add an iteration step to the DGM procedure. Because

cross sections are initially condensed with a guessed flux and subsequently condensed again with an improved flux, this iteration procedure is called *recondensation*.

When a flat in-mesh flux approximation is used, the DGM equations are fully consistent with the fine group transport problem. Thus, the recondensation procedure will converge to the true fine group flux [Zhu and Forget, 2011a]. However, this procedure was introduced not to fully compute the fine group flux but rather to improve condensed cross sections with a relatively few number of iteration steps.

In the multi-level approach of Sec. 1.2.2, this allows information from one level to be fed back to the previous level to improve the coarsened cross sections. For instance, if DGM is used on a core level calculation and unfolds the flux to the energy structure of the lattice calculation, corrections to account for reflective boundary conditions due to neighboring effects can be captured. If used on a lattice level calculation, unfolding to the energy structure of the self-shielding level, spatial self-shielding effects not previously captured can be picked up.

In previous work by Zhu and Forget [2011a], the recondensation procedure was found to be unstable in general. This was addressed by adding a flux update step after the unfolding step. Flux updates are single purely absorbing fine group sweeps using a fixed source built from the unfolded spectrum:

$$\begin{aligned} & \hat{\Omega} \cdot \nabla \psi_g^{\text{update}} + \Sigma_{t,g} \psi_g^{\text{update}} \\ &= \frac{1}{4\pi} \sum_{G'=1}^N \sum_{g' \in G'} \Sigma_{s,g' \rightarrow g} \phi_{g'} + \frac{\chi_g}{4\pi k} \sum_{G'=1}^N \sum_{g' \in G'} \nu \Sigma_{f,g'} \phi_{g'}. \end{aligned} \quad (1.56)$$

## 1.6 Fixed Point Iteration

The recondensation procedure discussed in Sec. 1.5.4 is an example of fixed point iteration. Details regarding this class of problems are presented here.

Fixed point iteration is the process of solving the equation  $x = \mathbb{A}x$ , where  $x$  is a vector and  $\mathbb{A}$  is some operator that can act on  $x$ . A given operator may have a unique fixed point, no fixed points, or multiple fixed points.

### 1.6.1 Picard Iteration

The most intuitive solution technique is Picard iteration or the sequence of successive approximations [Berinde, 2004]. The scheme starts with a guessed solution vector  $x^{(0)}$ , and subsequent iterates  $x^{(n)}$  are obtained by applying the operator:

$$x^{(n+1)} = \mathbb{A}x^{(n)}. \quad (1.57)$$

In practice, a solution is obtained when the difference between successive iterates, under some norm  $\|\cdot\|$ , is within a tolerance  $\epsilon$ :

$$\|x^{(n+1)} - x^{(n)}\| < \epsilon. \quad (1.58)$$

This procedure, however, is not guaranteed to converge in general. Rather, it requires that the operator  $\mathbb{A}$  be contractive. For any two vectors  $y_1$  and  $y_2$ , that is:

$$\|\mathbb{A}y_1 - \mathbb{A}y_2\| < \|y_1 - y_2\|. \quad (1.59)$$

This is equivalent to requiring the distance between successive Picard iterates decreases. Also, because at the solution  $x^*$ , the equality  $\mathbb{A}x^* = x^*$  holds true, this implies that each successive iterate more closely approximates the solution than the previous:

$$\|x^* - \mathbb{A}x^{(n)}\| < \|x^* - x^{(n)}\|. \quad (1.60)$$

An operator in which Picard iteration is convergent can be categorized as a  $\theta$ -contraction:

$$\|\mathbb{A}y_1 - \mathbb{A}y_2\| \leq \theta \|y_1 - y_2\| \quad \theta \in [0, 1]. \quad (1.61)$$

The value of  $\theta$  can be used to determine a bound on the convergence rate of Picard iteration, with smaller values of  $\theta$  leading to faster convergence.

### 1.6.2 Krasnoselskij Iteration

If an operator does not satisfy the contractive condition in Eq. 1.59, another iteration scheme is needed to solve the fixed point problem. The Krasnoselskij iteration [Krasnoselskij, 1955; Berinde, 2004] is one such iteration procedure. With  $\lambda \in (0, 1]$  as a fixed parameter, it is given by:

$$x^{(n+1)} = (1 - \lambda)x^{(n)} + \lambda \mathbb{A}x^{(n)}. \quad (1.62)$$

In the case of  $\lambda = 1$ , this reduces exactly to Picard iteration. More generally, Krasnoselskij is equivalent to Picard iteration where the operator is taken to be  $\mathbb{A}_\lambda = (1 - \lambda)\mathbb{I} + \lambda\mathbb{A}$ , with  $\mathbb{I}$  being the identity operator. This modified operator  $\mathbb{A}_\lambda$  requires a weaker condition on the operator  $\mathbb{A}$  for convergence of the iteration: that it be Lipschitzian [Berinde, 2004]. That is, there exists a finite  $L > 0$  such that:

$$\|\mathbb{A}y_1 - \mathbb{A}y_2\| < L\|y_1 - y_2\|. \quad (1.63)$$

In practice, the value of  $\lambda$  is a degree of freedom in an implementation of Krasnoselskij iteration. For a given operator, there exists some  $\lambda_{max}$  above which the iteration procedure will not be stable. In general,  $\lambda_{max}$  need not be the optimal choice of  $\lambda$  for the fastest convergence. In fact, in some cases where Picard iteration converges, Krasnoselskij iteration with  $\lambda < 1$  may converge faster.

Thus, there is also an optimal value  $\lambda_{opt}$  for which Krasnoselskij iteration converges the fastest. One must define the meaning of optimal in this context. In mathematics literature,  $\lambda_{opt}$  is obtained by minimizing the effective  $\theta$  from Eq. 1.61. However, this provides the optimal bound on the convergence rate but not necessarily the optimal convergence rate. For this study  $\lambda_{opt}$  will be considered the value of  $\lambda$  for which a solution within a given tolerance is achieved in the fewest iterations. Note that by this definition,  $\lambda_{opt}$  may be a function of not only the operator  $\mathbb{A}$  but also the starting guess  $x^{(0)}$ .

### 1.6.3 Other Schemes

Other fixed point iteration schemes exist. One such scheme is Mann iteration [Berinde, 2004], a straightforward extension of Krasnoselskij. In Mann,  $\lambda$  is replaced with  $a^{(n)} \in (0, 1]$  which is allowed to vary by iteration:

$$x^{(n+1)} = (1 - a^{(n)})x^{(n)} + a^{(n)}\mathbb{A}x^{(n)}. \quad (1.64)$$

For many problems, stability issues are magnified near the fixed point. Mann iteration allows larger steps to be taken when far from the fixed point and smaller steps near the solution to preserve stability.

Another iteration scheme is Ishikawa iteration [Berinde, 2004], which is a two-step procedure. Two parameter sequences  $a^{(n)}, b^{(n)} \in (0, 1]$  are used to arrive at the procedure definition:

$$\begin{aligned} y^{(n)} &= (1 - b^{(n)})x^{(n)} + b^{(n)}\mathbb{A}x^{(n)} \\ x^{(n+1)} &= (1 - a^{(n)})x^{(n)} + a^{(n)}\mathbb{A}y^{(n)}. \end{aligned} \quad (1.65)$$

Of course, many other iteration schemes exist, but these are not presented here.

## 1.7 Cross Sections Used in This Study

### 1.7.1 SHEMA361

The Santamarina-Hfaiedh Energy Mesh (SHEMA) was introduced by Hfaiedh and Santamarina [2005] as a 281-group optimized energy mesh to reduce the need for self-shielding calculations for low-lying resonances. The most common and significant isotopes encountered in reactor simulations, including actinides, fission products, absorbers, moderators/coolants, and structural materials were considered. The whole of these isotopes' resonance structure was considered up to 23 eV. Above this range, significant effects such as threshold reactions and other large resonances in U-238 were considered. The mesh sought to account for issues such as the mutual self-shielding effects of overlapping low-lying resonances.

The mesh was refined between 22.5 eV and 11.4 keV by Hébert and Santamarina [2008], raising the threshold energy below which the whole of the resonance structures of isotopes of interest were considered. This region was increased from 38 to 118 groups. The resulting group structure is denoted as SHEMA361 in this thesis.

A list of the energy boundaries of SHEMA361 is given in Appendix B.

### 1.7.2 NG2042

For the purpose of methods development, it was found that an energy mesh that sat between SHEMA361 and a true ultrafine mesh was needed. With only 361 groups, a library using the SHEMA361 energy mesh does not behave like an ultrafine group library, as it does not attempt to resolve resonances above 11.4 keV and only coarsely resolves resonances below this cutoff. A true ultrafine library, however, leads to many complications in calculations, including long computational run times and large memory requirements. Thus, the NG2042 energy mesh was introduced.

The NG2042 structure makes no attempt to optimize group selection and is certainly inadequate to resolve resonances. However, it has enough groups that libraries using it behave much like ultrafine libraries, without much of the unwanted storage and computational complications.

In the thermal region, NG2042 uses the TRESFIN 524-group energy block used in CEA's 11,276-group structure. Above thermal energies, groups are given equal lethargy widths of  $\Delta u = 1/480$ . The result is a 2042-group energy mesh.

### 1.7.3 UF14767

An ultrafine library dubbed UF14767 was developed for this study. CEA's 11,276-group structure was taken as the starting point. However, as this mesh was developed for use with ENDF/B-VI, it was necessary to increase the number of groups for the upper end of the resonance range when used with ENDF/B-VII data. Also, as some energy self-shielding effects were still seen, some further energy refinement was introduced. The resulting structure contains 14,767 groups, as described in Tab. 1.2. The thermal block uses the TRESFIN energy structure developed by CEA and tabulated in App. A. At higher energies, equal lethargy bins are used within broad energy bands.

Table 1.2: UF14767 energy mesh

Energy Range	Mesh Structure	Number of Groups
$E \leq 5.04348\text{eV}$	TRESFIN	524
$5.04348 < E \leq 51\text{eV}$	$\Delta u = 1/960$	2221
$51 < E \leq 203\text{eV}$	$\Delta u = 1/960$	1326
$203 < E \leq 1434\text{eV}$	$\Delta u = 1/1920$	3754
$1.434 < E \leq 200\text{keV}$	$\Delta u = 1/960$	4740
$0.2 < E \leq 19.64\text{MeV}$	$\Delta u = 1/480$	2202

Validation of this energy mesh is described in Sec. 2.1.

### 1.7.4 Cross Section Generation

All isotopic cross sections used in this study were generated in NJOY 99.336. Unless otherwise noted, cross sections were generated at 293.6 K. ENDF/B-VII.0 evaluated nuclear data was used for UF14767 library generation; ENDF/B-VII.1 was used for SHEM361 and NG2042 library generation.

The following NJOY modules were used in the library generation:

- moder – convert ENDF file from ASCII to binary
- reconr – construct point-wise cross sections from given resonance parameters
- broadr – Doppler broaden point-wise cross sections
- thermr – compute thermal scattering kernels using free gas models for non-moderators and  $S(\alpha, \beta)$  for moderators
- groupr – collapse point-wise cross sections into group-wise cross sections
- moder – convert group-wise ENDF file from binary to ASCII.

All cross sections in this study were generated at infinite dilution. No attempts to correct for self-shielding effects were made. For a sufficiently fine energy mesh, where self-shielding effects are fully resolved, the concept of dilution no longer means anything, and resulting cross sections are independent of the dilution cross section.

Sample NJOY inputs are included in Appendix C. These inputs show the input parameters used for each of the modules.

## Chapter 2

# DGM Applied to Ultrafine Energy Mesh

### 2.1 Validation of UF14767 Energy Mesh

The UF14767 library was validated by comparing to continuous energy Monte Carlo simulations in the recently developed OpenMC code [Romano and Forget, 2013]. ACE libraries for the Monte Carlo simulations were generated from the same point-wise ENDF files used to create the UF14767 cross section data using NJOY's acer module.

Two infinite media were considered, one representing a UO<sub>2</sub> LWR pin-cell and one representing a MOX pin-cell, described in detail in Sec. 2.2.1. Table 2.1 gives a summary of eigenvalues obtained from calculations with these materials. The continuous entries correspond to solutions in OpenMC with continuous energy cross sections; the multigroup entries correspond to solutions from a deterministic method using the UF14767 cross sections. Monte Carlo results have a reported standard deviation less than 5 pcm on the eigenvalues.

Table 2.1: Comparison of eigenvalues: UF14767 multigroup vs. continuous energy cross sections

Composition	Temperature	Multigroup	Continuous	Difference
UO <sub>2</sub>	293.6 K	1.35036	1.35219	-205 pcm
	600 K	1.32715	1.32817	-102 pcm
MOX	293.6 K	1.09824	1.10492	-668 pcm

In all cases considered, the multigroup results underpredict the eigenvalue computed with continuous energy data in Monte Carlo. Such systematic underprediction suggests that self-shielding phenomena are not fully accounted for. Furthermore, the reduction in error in the multigroup eigenvalue for the UO<sub>2</sub> mixture at higher temperature also suggests that errors are associated with self-shielding.

Figure 2.1 investigates this further, plotting the total cross section from the multigroup data against an inferred total cross section from Monte Carlo in part of the resonance range. The energy range

considered is 2.95 keV to 3.82 keV, corresponding to groups 6250 through 6500 in the UF14767 structure. Inferred cross sections are obtained by tallying total reaction rate and flux inside energy bins defined by the group bounds and taking their ratio. As is clearly seen, very good agreement is found in groups lying between resonances, but the multigroup data systematically overpredicts the resonance peaks. This confirms that self-shielding phenomena are not fully resolved in the UF14767 library.

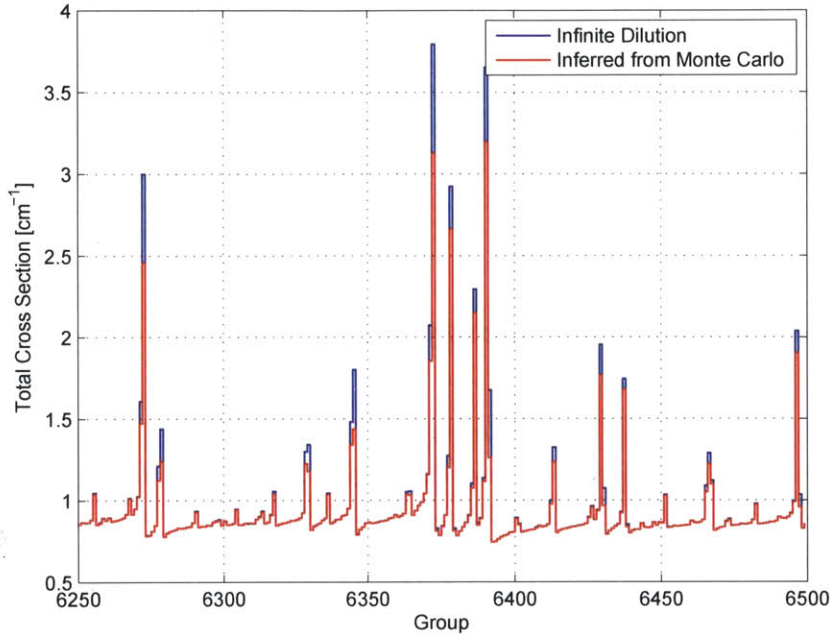


Figure 2.1: Comparison of UF14767 multigroup cross sections to inferred cross sections from Monte Carlo. Infinite dilution cross sections systematically overpredict resonance peaks.

It should be noted that the multigroup results presented in Tab. 2.1 used a single fission spectrum in the calculations. The spectrum was obtained by combining the isotopic fission spectra, weighted by the fission rate computed from a guessed flux. In this case, the guessed flux was taken to a Maxwellian at thermal energies, a narrow resonance model flux for resonant energies, and a fission spectrum at fast energies. The UO<sub>2</sub> results were found to be insensitive to the spectrum, with the eigenvalue changing by only 1 pcm if the U-235 spectrum is used. The MOX results, however, are highly sensitive to the spectrum. Using only the U-235 fission spectrum, the eigenvalue decreases by 250 pcm; using only the Pu-239 spectrum, the eigenvalue increases by 150 pcm. Thus, some of the error reported in the MOX mixture can be attributed to errors from the choice of the fission spectrum. However, most is still thought to originate from self-shielding.

In order to fully eliminate the need for self-shielding models, a finer group structure and/or an optimized energy mesh is needed. However, for the purposes of evaluating the DGM procedure in the context of an ultrafine energy mesh, this group structure is deemed to be sufficient.

## 2.2 DGM Results

### 2.2.1 Infinite Medium

The slowing down equation in an infinite homogenous medium was studied. Two compositions were considered, one representing a UO<sub>2</sub> pin-cell and one representing a MOX pin-cell. The pin-cells were assumed to have the geometry from the Mosteller benchmark for the Doppler reactivity coefficient [Mosteller et al., 1991], summarized in Tab. 2.2. This was converted to an infinite medium simply by volume weighting the number densities in each region. Densities were assumed to be 10.1 g/cc for the fuel, 6.55 g/cc for the clad, and 0.85 g/cc for the coolant regardless of composition. Temperature for all isotopes in the problem is taken to be 293.6 K. Uranium was assumed to be enriched to 3.9% for all cases; MOX fuel contained 80% uranium and 20% minor actinides (summarized in Tab. 2.3); clad was assumed to be natural zirconium; and the coolant was assumed to be non-borated light water. Resulting number densities are given in Tab. 2.4.

The reference solutions for these cases are taken to be the 14,767-group solutions. For the UO<sub>2</sub> case, the eigenvalue was found to be 1.35035; for the MOX case, 1.09824. Also used as comparisons to reference are the mean relative error (MRE) in flux and two-group total reaction rates:

$$\bar{\phi} \equiv \frac{\sum_{g=1}^{N_g} \phi_g}{N_g}$$

$$MRE \equiv \frac{\sum_{g=1}^{N_g} |\phi_g - \phi_g^{\text{ref}}|}{\bar{\phi} N_g} \quad (2.1)$$

$$RR_1 = \sum_{\substack{g \\ E_g \geq 0.625 \text{ eV}}} \Sigma_{tg} \phi_g$$

$$RR_2 = \sum_{\substack{g \\ E_g < 0.625 \text{ eV}}} \Sigma_{tg} \phi_g. \quad (2.2)$$

For all DGM results presented, the starting spectrum guess was taken to be the narrow resonance approximation flux ( $\phi \sim 1/E \cdot \sigma_t(E)$ ) in the resonance region, a Maxwellian in the thermal region, and the fission spectrum for the fast region.

For all results shown in this section, the Discrete Legendre Orthogonal Polynomials (DLOPs), presented in Sec. 1.4.1, were used. Due to accumulation of roundoff error, DLOPs cannot be taken to arbitrarily high expansion orders. It was found that stable convergence could be attained with DLOPs as high as 60<sup>th</sup> order. However, by using Discrete Cosine Transforms (DCTs), presented in Sec. 1.4.2, much higher expansion orders can be used. Expansions with order 100 and higher were found to be stable.

Table 2.2: Geometry specifications for Mosteller benchmark pin-cell

Measurement	Value (cm)
Pitch	1.26209
Fuel OR	0.39306
Clad OR	0.45802

Table 2.3: Minor actinide concentrations used in test problems

Isotope	Relative Concentration
Np-237	0.05343
Pu-238	0.02636
Pu-239	0.48408
Pu-240	0.21778
Pu-241	0.10506
Pu-242	0.06222
Am-241	0.03368
Am-243	0.01740

Table 2.4: Number densities for test problems

Isotope	Concentration [ $\text{a}/\text{b}\cdot\text{cm}$ ]	
	UO <sub>2</sub>	MOX
H-H <sub>2</sub> O	0.0333426	0.0333426
O-16	0.0303996	0.0303996
Zr-0	0.0047264	0.0047264
U-235	0.0002677	0.0002142
U-238	0.0065964	0.0052771
Np-237	-	0.0000734
Pu-238	-	0.0000362
Pu-239	-	0.0006646
Pu-240	-	0.0002990
Pu-241	-	0.0001442
Pu-242	-	0.0000854
Am-241	-	0.0000462
Am-243	-	0.0000239

As discussed in Sec. 1.5.4, previous work found that flux updates—or fine group fixed source sweeps—were needed at the end of each recondensation step in order to attain stability of the procedure. When applying DGM to the ultrafine energy mesh, it was found that a single flux update was not enough to ensure stability. For the results in this section, three flux updates were needed. With such a fine energy mesh, the addition of these extra flux updates is very costly.

The rate of convergence was found to be very sensitive to the mapping. Consider two example mappings used with the UO<sub>2</sub> case, summarized in Tab. 2.5. Mapping 1 uses a constant expansion order in each coarse group, representing a 14,767 → 493 group mapping. Mapping 2 uses a constant expansion order within each coarse group in a given energy range, but allows the order to change in different energy ranges, leading to a 14,767 → 366 group mapping.

Table 2.5: Example coarse-to-fine group mappings

Energy Range	Fine Groups per Coarse Group	
	Mapping 1	Mapping 2
$E \leq 5.04348 \text{ eV}$	30	25
$5.04348 < E < 51 \text{ eV}$	30	25
$51 < E \leq 203 \text{ eV}$	30	30
$203 < E \leq 1434 \text{ eV}$	30	50
$1.434 < E \leq 200 \text{ keV}$	30	50
$0.2 < E \leq 19.64 \text{ MeV}$	30	50

Despite higher order expansions and thus fewer coarse groups, Mapping 2 is seen to far outperform Mapping 1 after the first iteration, as shown in Tab. 2.6 and Tab. 2.7. Similar results were seen with the MOX case, shown in Tab. 2.8 and Tab. 2.9.

Table 2.6: Convergence for UO<sub>2</sub> case, Mapping 1

Iteration	$k$ Error (pcm)	Flux MRE	$RR_1$ Rel. Error	$RR_2$ Rel. Error
1	279.910	6.5969E-03	3.2147E-03	-1.1031E-02
2	49.492	5.6616E-04	3.6906E-04	-5.9286E-04
3	17.877	1.3616E-04	4.8322E-05	2.2975E-05
4	5.359	4.0390E-05	1.1468E-05	1.6003E-05

Table 2.7: Convergence for UO<sub>2</sub> case, Mapping 2

Iteration	$k$ Error (pcm)	Flux MRE	$RR_1$ Rel. Error	$RR_2$ Rel. Error
1	198.184	5.6379E-03	2.5087E-03	-1.0344E-02
2	-3.342	3.2436E-04	2.0430E-04	-6.6638E-04
3	0.080	1.75801E-05	1.0306E-05	-3.1409E-05
4	0.029	1.0930E-06	5.7751E-07	-1.6392E-06

Table 2.8: Convergence comparisons for MOX case, Mapping 1

Iteration	$k$ Error (pcm)	Flux MRE	$RR_1$ Rel. Error	$RR_2$ Rel. Error
1	70.455	5.0077E-03	1.3747E-03	-4.1587E-03
2	18.025	2.3345E-04	8.1386E-05	2.3909E-04
3	5.450	5.4569E-05	1.7576E-05	8.3621E-05
4	1.283	1.2992E-05	4.4187E-06	1.9910E-05

Table 2.9: Convergence comparisons for MOX case, Mapping 2

Iteration	$k$ Error (pcm)	Flux MRE	$RR_1$ Rel. Error	$RR_2$ Rel. Error
1	139.582	2.1709E-03	2.1143E-04	-1.7948E-04
2	-2.526	1.6147E-05	-9.0651E-07	-4.4138E-05
3	-0.023	4.4438E-07	-1.2296E-07	-3.0517E-07
4	-0.004	3.8579E-08	-1.2539E-08	-7.7328E-08

With this procedure, significant improvement in the flux, reaction rates, and eigenvalue were achieved with very few iterations. With an appropriate choice of a group map, only two to three recondensation steps recondensation steps were needed to yield results with very small deviation from the reference solution.

### 2.2.2 1-D Discrete Ordinates

In order to demonstrate that DGM could be applied to spatial problems with an ultrafine energy mesh, a very simple 1-D problem is modeled. Consider a slab reactor, infinite in two dimensions, varying in the third dimension as an infinite lattice of fuel elements. This can be modeled as two slabs with reflective boundary conditions. A pictorial representation of this geometry is given in Fig. 2.2.

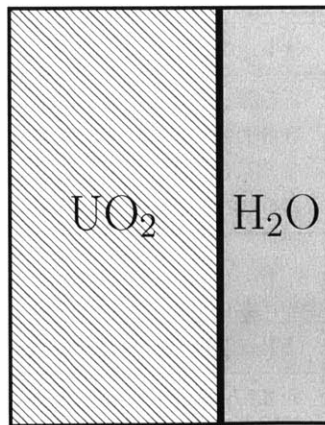


Figure 2.2: Geometry for simple slab 1-D pin-cell test problem

The problem considered is intended to represent the Mosteller benchmark pin-cell used in Sec. 2.2.1. The fuel region contains 3.9% enriched  $\text{UO}_2$  at 10.1 g/cc, and the coolant region contains water at 0.85

g/cc. Isotopic concentrations of the materials are given in Tab. 2.10. The width of the  $\text{UO}_2$  slab is 0.393 cm; the width of the water slab is 0.238 cm.

Table 2.10: Isotopic concentrations of the materials in 1-D pin-cell

Isotope	Concentration [#/b-cm]	
	$\text{UO}_2$	Water
H-H <sub>2</sub> O	-	0.0669
O-16	0.0446	0.0335
U-235	0.0006691	-
U-238	0.0216	-

The problem was solved using the discrete ordinates method [Lathrop and Carlson, 1964; Lewis and Miller, 1993]. An 8-point Gauss-Legendre angular quadrature was used. The step difference spatial discretization was employed with 8 mesh points in each slab. The group map was chosen to have approximately 50 fine groups in each coarse group, resulting in a  $14767 \rightarrow 295$  group map. In order to attain stability in the recondensation procedure, four flux updates were needed. Table 2.11 shows a summary of the eigenvalue error for the first few iterations. As with the infinite medium results, the eigenvalue is seen to improve dramatically in only a few recondensation steps. The reference eigenvalue is 1.25068.

Table 2.11: 1-D slab pin-cell DGM results

DGM Iteration	$k$	$k$ Error [pcm]
1	1.05069	-19999
2	1.25154	86
3	1.25065	-3

For this problem, Tab. 2.12 shows the profile of computational time spent in each aspect of a recondensation step for the first few iterations. Each recondensation step includes collapsing the fine group cross sections into coarse group cross sections and associated moments, solving the coarse group transport equation, solving the higher order equations, and performing flux updates. This process was implemented in Fortran 2003 and was run on the MIT computational cluster Kilkenny. Note that the code was not written to be performance-oriented, and so timing results are likely not optimal. However, the results certainly qualitatively characterize the computational expense well.

It is apparent that the bulk of the computational effort expended to solve the DGM equations is in computing the moments and in the flux updates. The coarse group transport equation and the higher order moment equations are of negligible cost in comparison.

Table 2.12: Timing summary of recondensation steps for 1-D DGM problem. Steps include moment generation, solving the coarse group transport equation, solving the higher order equations, and flux updates.

Iteration	Computational Time [s]			
	Moments	Coarse TE	HO Eqns	Updates
1	364	0.5	5	456
2	360	0.5	5	458
3	361	0.5	5	455

## 2.3 Complications and Concerns

This study successfully demonstrated that DGM can be applied to an ultrafine energy mesh. However, it highlighted four problems that must be addressed in order to make DGM a viable means of alleviating self-shielding approximations.

- 1. UF14767 ultrafine energy mesh is not sufficient to resolve self-shielding phenomena.
- 2. Memory requirements of using an ultrafine energy mesh are enormous.
- 3. Computing DGM moments is very costly.
- 4. Flux updates needed for stability are prohibitively expensive.

In the validation of the UF14767 ultrafine energy mesh, it was found that errors arising from inadequate self-shielding resolution were present. In order to use DGM to eliminate self-shielding, the fine group energy mesh must sufficiently resolve the resonances. This may require the addition of groups into the structure. Alternatively, a departure from equal lethargy bins to an optimized group structure could keep the number of groups at a tractable number. However, in a group optimization process, care must be taken to ensure the resulting energy mesh is not problem dependent.

Although not previously discussed in this chapter, this study highlighted the vast memory requirements of an explicit ultrafine energy mesh in a deterministic calculation. As discussed in Sec. 1.3.2, an explicit scattering matrix with the UF14767 structure for a single material containing hydrogen requires nearly 1 GB of memory to store in double precision. As more materials are added and higher order scattering is introduced, this storage requirement may become prohibitive. In many of the ultrafine energy mesh implementations discussed in Sec. 1.3.1, approximations to and alternate representations of the scattering kernel were made. These included computing elastic scattering

sources on the fly, separating the inelastic scattering, using the submoment expansion method, and many others. DGM may offer another approach, allowing the scattering matrix to contain many fewer groups than the collision and streaming terms. This is a subject left to future work.

The bulk of the expense in computing the DGM moments in an ultrafine energy mesh is in the computation of the scattering matrix's moments. Any work to reduce the memory footprint of the scattering matrix would likely also reduce the cost associated with computing the moments. Also, computing moments is a local computational effort; that is, it does not require information of neighboring spatial regions or even of other moments. Thus, the process is easily parallelizable.

Finally, the addition of more flux updates is not a good alteration to the recondensation process. With more moments, the advantage of carrying out the transport calculation on the coarse energy mesh is removed. Also, the cost associated with fine group sweeps at the ultrafine mesh level is prohibitive. Thus, work is needed to improve the stability of the recondensation procedure without turning to flux updates. This work is the subject of the remainder of this thesis.

# Chapter 3

## Stability of DGM Procedure

### 3.1 Simplest Example of Stability Issues

#### 3.1.1 Description

In order to study the stability of the DGM procedure, consider the simplest possible DGM problem: two fine groups mapped to a single coarse group in an infinite medium. For simplicity, there is no up-scattering and all fission neutrons are born in the fast group. For this problem, the fine group equations are:

$$\begin{aligned}\Sigma_{t,1}\phi_1 &= \Sigma_{s,1 \rightarrow 1}\phi_1 + \frac{1}{k}(\nu\Sigma_{f,1}\phi_1 + \nu\Sigma_{f,2}\phi_2) \\ \Sigma_{t,2}\phi_2 &= \Sigma_{s,1 \rightarrow 2}\phi_1 + \Sigma_{s,2 \rightarrow 2}\phi_2.\end{aligned}\tag{3.1}$$

The discrete basis set is chosen to be Discrete Legendre Orthogonal Polynomials:

$$\begin{aligned}\xi_0 &= [1 \quad 1] \\ \xi_1 &= [1 \quad -1].\end{aligned}\tag{3.2}$$

The flux moments are then:

$$\begin{aligned}\varphi_0 &= \phi_1 + \phi_2 \\ \varphi_1 &= \phi_1 - \phi_2,\end{aligned}\tag{3.3}$$

and the unfolded flux is:

$$\begin{aligned}\phi_1 &= \frac{1}{2}(\varphi_0 + \varphi_1) \\ \phi_2 &= \frac{1}{2}(\varphi_0 - \varphi_1).\end{aligned}\tag{3.4}$$

The DGM equations are thus:

$$\begin{aligned}\Sigma_{t,0,G}\varphi_0 &= \Sigma_{s,0,G}\varphi_0 + \frac{1}{k}\nu\Sigma_{f,G}\varphi_0 \\ \Sigma_{t,0,G}\varphi_1 + \delta_{1,G}\varphi_0 &= \Sigma_{s,1,G}\varphi_0 + \frac{1}{k}\nu\Sigma_{f,G}\varphi_0,\end{aligned}\tag{3.5}$$

where the DGM cross sections are given by:

$$\Sigma_{t,0,G} = \frac{\Sigma_{t,1}\phi_1 + \Sigma_{t,2}\phi_2}{\phi_1 + \phi_2}\tag{3.6}$$

$$\delta_{1,G} = \frac{(\Sigma_{t,1} - \Sigma_{t,0,g})\phi_1 - (\Sigma_{t,2} - \Sigma_{t,0,g})\phi_2}{\phi_1 + \phi_2}\tag{3.7}$$

$$\Sigma_{s,0,G} = \frac{(\Sigma_{s,1 \rightarrow 1} + \Sigma_{s,1 \rightarrow 2})\phi_1 + \Sigma_{s,2 \rightarrow 2}\phi_2}{\phi_1 + \phi_2}\tag{3.8}$$

$$\Sigma_{s,1,G} = \frac{(\Sigma_{s,1 \rightarrow 1} + \Sigma_{s,1 \rightarrow 2})\phi_1 - \Sigma_{s,2 \rightarrow 2}\phi_2}{\phi_1 + \phi_2}\tag{3.9}$$

$$\nu\Sigma_{f,G} = \frac{\nu\Sigma_{f,1}\phi_1 + \nu\Sigma_{f,2}\phi_2}{\phi_1 + \phi_2}.\tag{3.10}$$

Because this is an eigenproblem, the solution  $\begin{bmatrix} \phi_1 & \phi_2 \end{bmatrix}^T$  has a multiplicative degree of freedom. Thus, it can be fully defined with the thermal-to-fast flux ratio  $f = \phi_2/\phi_1$ .

The standard solution methodology is to cast the DGM problem as a fixed-point iteration. The DGM equations take guesses of  $\phi_1$  and  $\phi_2$ —or equivalently  $f$ —as an input to collapse the cross sections with Eqs. 3.6–3.10. They are then solved to produce updated values,  $\tilde{\phi}_1$  and  $\tilde{\phi}_2$  or  $\tilde{f}$ . The DGM operator is denoted as  $\mathbb{D}$ . The updated values can be used to define the input for the next iteration. The solution is achieved when  $f = \tilde{f}$  within some tolerance.

The most intuitive fixed point iteration scheme is Picard iteration, described in Sec. 1.6.1:

$$f^{(n+1)} = \mathbb{D}(f^{(n)}) \equiv \tilde{f}^{(n)}.\tag{3.11}$$

### 3.1.2 Numerical Examples

Now, consider a numerical example with this simple problem. Take the fine group cross sections to be:

$$\begin{aligned}\Sigma_{t,1} &= 1 \text{ cm}^{-1} & \Sigma_{t,2} &= 2 \text{ cm}^{-1} \\ \Sigma_{s,1 \rightarrow 1} &= \Sigma_{s,1 \rightarrow 2} = \Sigma_{s,2 \rightarrow 2} = 0.3 \text{ cm}^{-1} \\ v\Sigma_{f,1} &= v\Sigma_{f,2} = 0.5 \text{ cm}^{-1}.\end{aligned}\tag{3.12}$$

Using  $f_0 = 1$  as the starting seed for Picard iteration, Tab. 3.1 gives the thermal-to-fast flux ratio and eigenvalue for the first 15 iterates. The true solution is  $f = 0.1765$  and  $k = 0.8403$ . Convergence to  $10^{-5}$  on eigenvalue is obtained in 39 iterations.

Table 3.1: Picard iterates for convergent  $2 \rightarrow 1$  group infinite medium DGM procedure

Iteration	$f$	$k$
1	0.0345	0.4762
2	0.3498	1.1278
3	0.0938	0.6785
4	0.2564	0.9775
5	0.1290	0.7516
6	0.2172	0.9115
7	0.1497	0.7912
8	0.1980	0.8784
9	0.1615	0.8132
10	0.1880	0.8609
11	0.1682	0.8254
12	0.1827	0.8515
13	0.1719	0.8322
14	0.1799	0.8464
15	0.1740	0.8359

Next, consider a second problem in which the same cross sections are used, changing only the value of  $\Sigma_{t,2}$ :

$$\Sigma_{t,2} = 3 \text{ cm}^{-1}.\tag{3.13}$$

Again using  $f_0 = 1$  as the starting seed for Picard iteration, Tab. 3.2 gives the thermal-to-fast flux ratio and eigenvalue for the first 15 iterates. The true solution is  $f = 0.1111$  and  $k = 0.7937$ . Rather than approaching this solution, the iterates quickly diverge. Negative fluxes are seen after only a single iteration.

Table 3.2: Picard iterates for non-convergent  $2 \rightarrow 1$  group infinite medium DGM procedure

Iteration	$f$	$k$
1	-0.0909	0.3226
2	1.8571	2.9412
3	-0.0631	0.2639
4	1.0534	2.0408
5	-0.0897	0.3165
6	1.8036	2.8845
7	-0.0650	0.2660
8	1.0881	2.0820
9	-0.0888	0.3128
10	1.7664	2.8449
11	-0.0663	0.2676
12	1.1134	2.1120
13	-0.0882	0.3102
14	1.7384	2.8150
15	-0.0673	0.2688

To understand this behavior, consider the stability requirements of Picard iteration, as presented in Sec. 1.6.1. The requirement that the operator be contractive is equivalent to requiring the spectral radius of the operator be less than unity. For a univariate fixed point scheme such as this one, the spectral radius  $\rho$  is the magnitude of the derivative of the output  $y$  with respect to the input  $x$ :

$$\rho = \left| \frac{dy}{dx} \right|. \quad (3.14)$$

By evaluating the DGM operator over a full range of input  $f$  values, a plot of input versus output and the derivative can be generated. Figure 3.1 shows this plot for the first case, with  $\Sigma_{t,2} = 2 \text{ cm}^{-1}$ ; Fig. 3.2 shows this plot for the second case, with  $\Sigma_{t,2} = 3 \text{ cm}^{-1}$ .

In these plots, the solution is the intersection of  $f(x)$  and the line  $y = x$ . At the solution, for the first case, the magnitude of the derivative is seen to be less than unity; thus, a Picard iteration procedure starting in a neighborhood about the solution is expected to converge to the solution.

For the second case, the magnitude of the derivative is seen to be greater than unity at the solution; thus, the scheme is unstable, and Picard iteration is not expected to converge to the solution from any starting guess.

Even in this extremely simple example, stability issues pertaining to the DGM recondensation procedure can be seen. For any physical problem, without modification, the DGM procedure cannot be expected to be stable in general. Next, means of improving the stability will be presented.

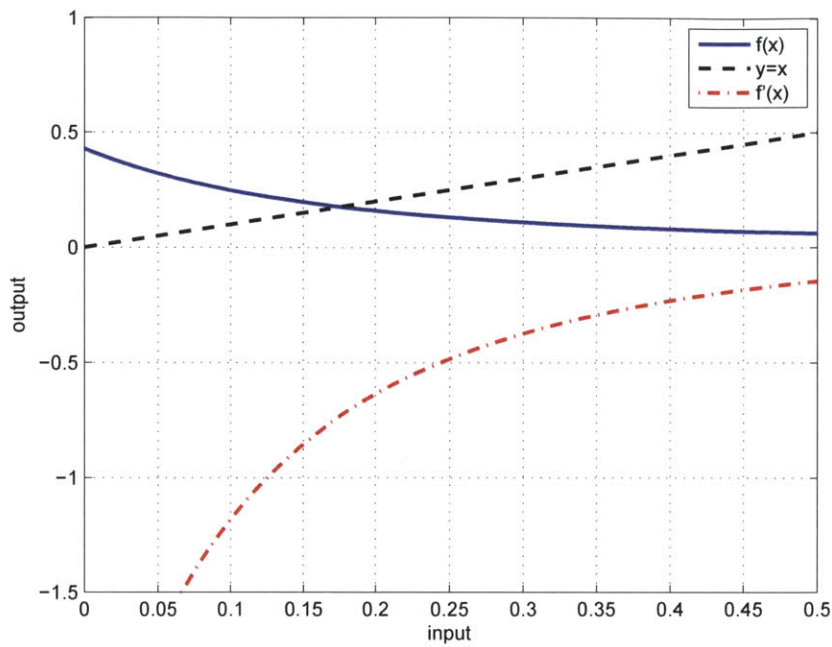


Figure 3.1: Input versus output thermal to fast flux ratios for stable DGM case

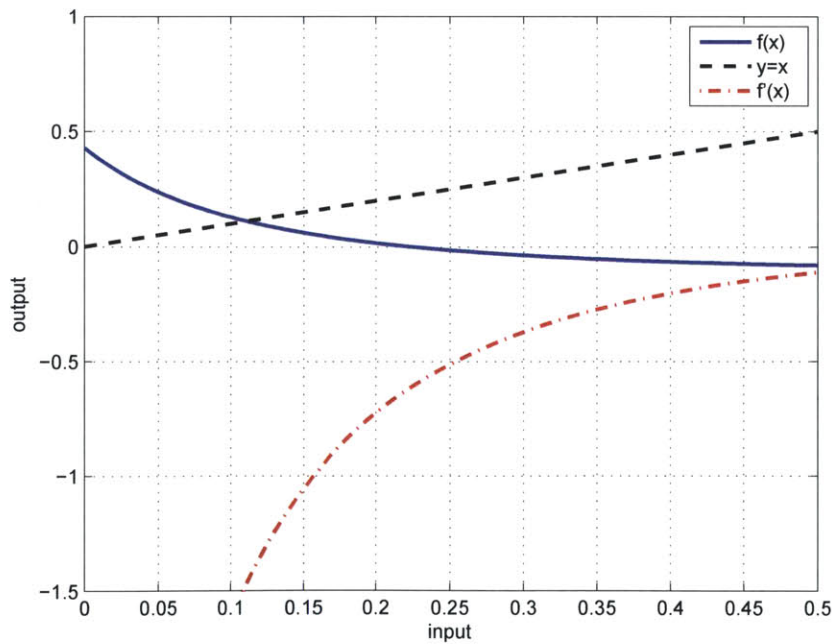


Figure 3.2: Input versus output thermal to fast flux ratios for unstable DGM case

## 3.2 Improving Stability of Iteration Scheme

### 3.2.1 Flux Updates

In past work [Zhu and Forget, 2011a], stability concerns were addressed through the use of flux updates, described in Sec. 1.5.4. These flux updates add a fine group fixed source sweep to the operator, making Picard iteration stable. The unfolded flux from the solution of the DGM equations is used to build a fixed scattering and fission source, and a transport sweep is performed to obtain a new flux. For the simple problem presented in Sec. 3.1.1, the flux update is simplified:

$$\begin{aligned}\phi_1^{\text{update}} &= \frac{\Sigma_{s,1 \rightarrow 1}\phi_1 + \frac{1}{k}(\nu\Sigma_{f,1}\phi_1 + \nu\Sigma_{f,2}\phi_2)}{\Sigma_{t,1}} \\ \phi_2^{\text{update}} &= \frac{\Sigma_{s,1 \rightarrow 2}\phi_1 + \Sigma_{s,2 \rightarrow 2}\phi_2}{\Sigma_{t,2}}.\end{aligned}\tag{3.15}$$

When a flux update is added to the DGM operator in the simple example, the previously unstable case, with  $\Sigma_{t,2} = 3 \text{ cm}^{-1}$ , stably converges to the true solution. Table 3.3 shows the iterate values of  $f$  and  $k$ . Figure 3.3 shows the input versus output and derivative plot. The magnitude of the derivative at the solution is less than unity, and so the procedure is expected to be convergent, as is observed in practice.

Flux updates, however, have several problems. For difficult problems, such as those presented in Ch. 2, several flux updates are needed for stability. Especially in the limit of large numbers of groups, this process can be quite computationally expensive. Also, performing large numbers of fine group sweeps is essentially solving the problem classically, removing the benefit of the DGM method.

### 3.2.2 Krasnoselskij Iteration

A simple potential fix for DGM without turning to flux updates or modifying the operator in any way is the Krasnoselskij iteration, presented in Sec. 1.6.2. For a general DGM problem, with eigenvector  $\psi$  and  $\tilde{\psi} \equiv \mathbb{D}(\psi)$ , this is:

$$\psi^{(n+1)} = (1 - \lambda)\psi^{(n)} + \lambda\tilde{\psi}^{(n)}.\tag{3.16}$$

Consider again the second case of the simple example, with  $\Sigma_{t,2} = 3 \text{ cm}^{-1}$ . Using  $\lambda = 0.7$ , the procedure is found to stably converge to the true solution. With a convergence criteria of  $10^{-5}$  on eigenvalue, 39 iterations are required to reach the solution. Table 3.4 gives the first 15 iterate values of  $f$  and  $k$ .

Table 3.3: Picard iterates for  $2 \rightarrow 1$  group infinite medium DGM procedure with flux update

Iteration	$f$	$k$
1	0.3226	0.0532
2	0.9687	0.1315
3	0.7493	0.1059
4	0.8061	0.1126
5	0.7902	0.1107
6	0.7946	0.1112
7	0.7934	0.1111
8	0.7937	0.1111
9	0.7936	0.1111
10	0.7937	0.1111
11	0.7936	0.1111
12	0.7937	0.1111

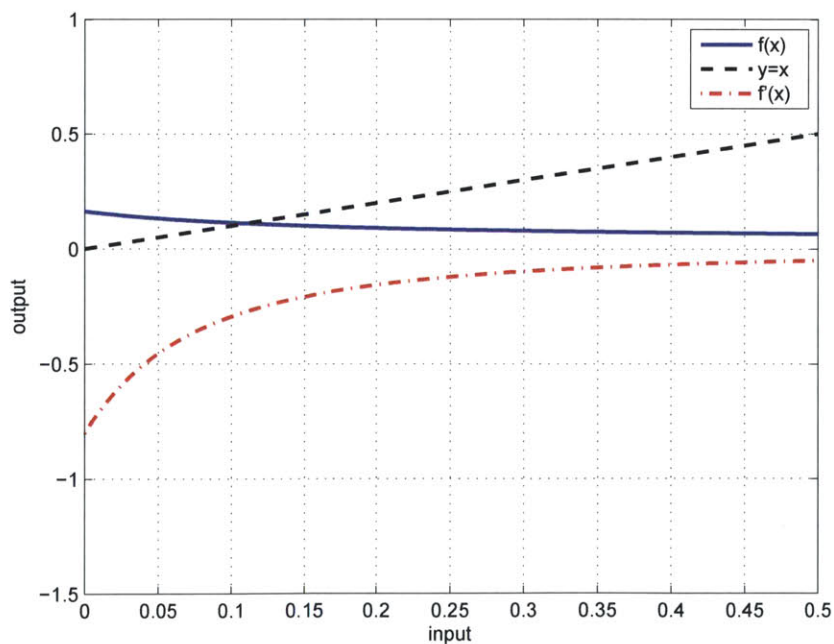


Figure 3.3: Input versus output thermal to fast flux ratios for DGM with flux update

Table 3.4: Krasnoselskij iterates for  $2 \rightarrow 1$  group infinite medium DGM procedure

Iteration	$f$	$k$
1	0.3226	0.2364
2	0.5954	0.0663
3	0.9210	0.1564
4	0.7032	0.0853
5	0.8608	0.1339
6	0.7444	0.0962
7	0.8307	0.1234
8	0.7662	0.1026
9	0.8143	0.1179
10	0.7782	0.1063
11	0.8052	0.1149
12	0.7850	0.1084
13	0.8002	0.1132
14	0.7888	0.1096
15	0.7973	0.1123

In the same simple example, if all cross sections are held constant aside from  $\Sigma_{t,2}$ , larger values of  $\Sigma_{t,2}$  require smaller values of  $\lambda$  for stability. For example, a value of  $\Sigma_{t,2} = 100 \text{ cm}^{-1}$  requires  $\lambda \leq 0.02$ . Although choosing a very small value of  $\lambda$  ensures stability for any conditions, it also greatly slows convergence. Table 3.5 summarizes the iterations required to reach the solution for various choices of  $\Sigma_{t,2}$  and  $\lambda$ .

Consider now a larger problem, that of an infinite medium of a UO<sub>2</sub>-water mixture with the SHEM361 group structure. Number densities are given in Tab. 3.6. The coarse-to-fine group map is taken to be a 361 → 12 group map with approximately 30 fine groups in each coarse group. Without flux updates, this problem is unstable with Picard iteration. However, using the Krasnoselskij iteration procedure, convergence can be achieved. The maximum stable value of  $\lambda$  is found to be 0.025. To achieve a convergence of  $10^{-5}$  on eigenvalue, 1610 iterations are required. Thus, while Krasnoselskij allows for stability in the DGM recondensation procedure, the very small values of  $\lambda$  required for stability with an arbitrary group map on realistic data lead to very high computational expense.

Table 3.5: Iterations required for convergence of Krasnoselskij procedure

$\Sigma_{t,2} [\text{cm}^{-1}]$	$\lambda = 1$	$\lambda = 0.7$	$\lambda = 0.2$	$\lambda = 0.02$
2	39	9	29	256
3	-	39	23	214
10	-	-	25	123
100	-	-	-	68

Table 3.6: Number densities used in SHEM361 infinite medium example problem

Isotope	Number Density [a/b-cm]
H-1 ( $\text{H}_2\text{O}$ )	0.029754258
O-16	0.034689322
U-235	0.0002575585
U-238	0.009648538

### Modified Krasnoselskij Iteration

In the 361-group infinite medium example problem, for cases in which the DGM procedure did not converge, large errors were seen to develop in groups that contain resonances. In these groups, fluxes are expected to be near zero. Fluxes are seen to become negative in these groups and, rather than be corrected by the iteration scheme, lead to increasingly large errors.

Consider the previously used simple problem of an infinite medium consisting of a  $\text{UO}_2$ -water mixture with the SHEM361 group structure. Using the group mapping of  $361 \rightarrow 12$  with 30 fine groups in each coarse group and  $\lambda = 0.15$ , this behavior is demonstrated in Fig. 3.4. At iteration 15, a small negative flux is observed. At the next iteration, rather than approaching a physical solution, the solution is seen to blow up near the negative flux. More negative fluxes are also seen to develop in other resonant groups.

This observation leads to a possible modification of the Krasnoselskij iteration procedure for improved performance. Because the instabilities appear to be driven by groups with large cross sections, a smaller value of  $\lambda$  can be applied to the flux in those groups, whereas larger values can be applied to the non-resonant groups.

To apply this procedure, one needs to determine the number of sets to split the fine groups into that would have a unique  $\lambda$  value—with these sets being dubbed “levels” for the purposes of this study. Next,  $\lambda$  values must be selected for each level.

This procedure was applied to the same infinite medium problem. Three cases are considered: a one-level, a two-level, and a four-level modified Krasnoselskij iteration procedure. Table 3.7 summarizes the values of  $\lambda$  used for each level in the iteration procedure. The values were chosen by trial and error, maximizing  $\lambda$  while maintaining stability of the procedure.

Figure 3.5 shows a plot of eigenvalue versus iteration for each of the three cases. These results show that applying different values of  $\lambda$  to each fine group does not improve estimates of the eigenvalue at early iterations. However, the modified procedure does allow the eigenvalue to converge to the reference solution in less total iterations. No choice of  $\lambda$  values in this procedure allowed for a converged solution to be obtained in less than the 150-250 iterations shown for the two- and four-level results.

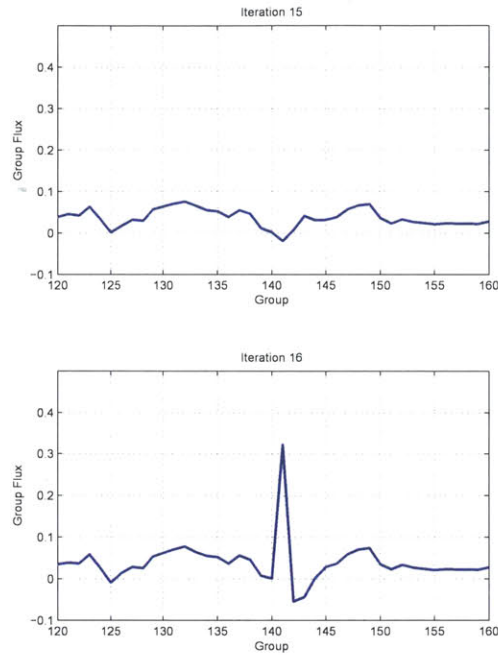


Figure 3.4: Instability in DGM reconensation procedure occurring in resonance group

Table 3.7:  $\lambda$  values for modified Krasnoselskij iteration procedures

Groups	One-Level	Two-Level	Four-Level
$\Sigma_{tg} < 0.01 \Sigma_{t,max}$	0.025	1.0	1.0
$\Sigma_{tg} \in [0.01, 0.05) \Sigma_{t,max}$	0.025	0.025	0.5
$\Sigma_{tg} \in [0.05, 0.20) \Sigma_{t,max}$	0.025	0.025	0.2
$\Sigma_{tg} > 0.20 \Sigma_{t,max}$	0.025	0.025	0.025

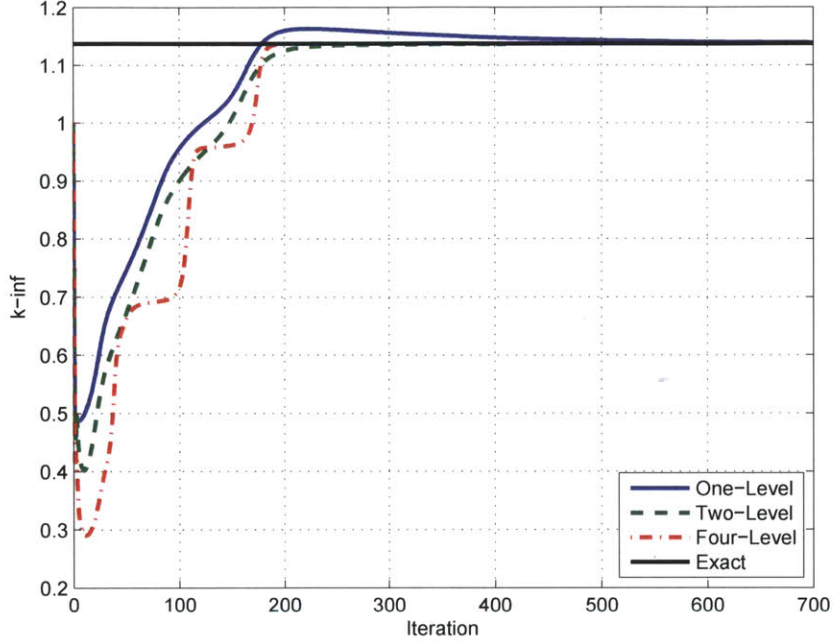


Figure 3.5: Eigenvalue versus iteration for modified Krasnoselskij procedure

It should be noted that the four-level procedure produces a curious convergence behavior. The eigenvalue plateaus with respect to iteration at a few points in the procedure and improves with respect to the reference very quickly between these plateaus. This demonstrates that by selecting  $\lambda$  in a piecewise manner as done here causes the error associated with each subset of groups to be reduced independently. Thus, during the iteration procedure, the dominant source of error in the eigenvalue shifts from one subset of groups to the next.

Because of the large number of iterations required to achieve a close approximation of the reference, the modified Krasnoselskij is not a viable solution methodology. Stability issues arising from large cross sections must be addressed through the choice of group map rather than through carefully chosen  $\lambda$  values.

A similar procedure as the one presented here could be made by applying a carefully selected value of  $\lambda$  in each coarse group rather than each fine group. This would require coarse groups containing resonances to use very small  $\lambda$  values, and so the issue of slow convergence would not be obviated. Although not studied in this work, such a procedure could provide a marginal benefit to a compatible iteration scheme.

### 3.2.3 Group Map

In the DGM method, a degree of freedom is the selection of the mapping between the fine and coarse group structures. In Ch. 2, the mapping was shown to greatly influence the convergence rate of the

recondensation procedure. The observed behavior did not show a simple relationship between the number of coarse groups and the convergence rate. However, because of the use of flux updates in this study, the impact of the group map on stability was not considered.

Without flux updates, the selection of the group map is of great importance to the stability of the method. As seen in the preceding simple 2 group example, relatively small disparities in cross sections can lead to instability. Consider now a 10 group infinite medium problem as an illustrative example to examine how the selection of the group map can address this issue.

In this example, the total cross section is taken to have a large cross section in groups 5-7—analogous to a resonance—and a much smaller but noisy cross section in the other groups, as shown in Fig. 3.6. The fission and scattering sources were taken to be as simple as possible so as not to influence the results.

Figure 3.7 shows two potential group maps with three coarse groups. The first is an arbitrarily selected map, which includes an enormous range of magnitudes of cross sections in the second coarse group. The second map still uses three coarse groups, but shifts the boundaries such that the resonance analog is fully contained within the second coarse group.

In both cases, Krasnoselskij iteration can be used to stably converge to the known solution. In the first mapping, the maximum stable choice of the  $\lambda$  parameter was found by trial and error to be 0.23. The fastest converging choice was found to be 0.22, leading to convergence of  $10^{-5}$  on the eigenvalue in 64 iterations. In the second mapping,  $\lambda$  values as high as 0.9 are seen to lead to convergence, and a choice of 0.7 leads to convergence in only 17 iterations. This clearly shows a strong relationship between the mapping and the efficiency of the algorithm.

Although this simple illustrative example demonstrates the necessity of a strong choice of a group map, it does not fully define an algorithm to do so. However, these ideas can easily be applied to more substantial problems to create such an algorithm.

With this in mind, possible group maps were investigated with a trial and error methodology. It was found that disparities in cross sections inside coarse groups more strongly affect stability via their ratio than a simple difference. Thus, a group mapping algorithm should seek to limit the ratio of the minimum to maximum total cross section inside a coarse group.

It was found that regions with small cross sections do not greatly affect the stability of the solution scheme, even if the ratio of cross sections becomes large. This is a fairly intuitive result, as regions with small reaction rates are unlikely to greatly influence the overall solution. Thus, a group mapping algorithm should not apply the limit on the ratio below a threshold cross section.

In Ch. 2, the maximum number of fine groups per coarse group without compromising stability was sought. Using Discrete Legendre Orthogonal Polynomials, a loss of orthogonality is observed when

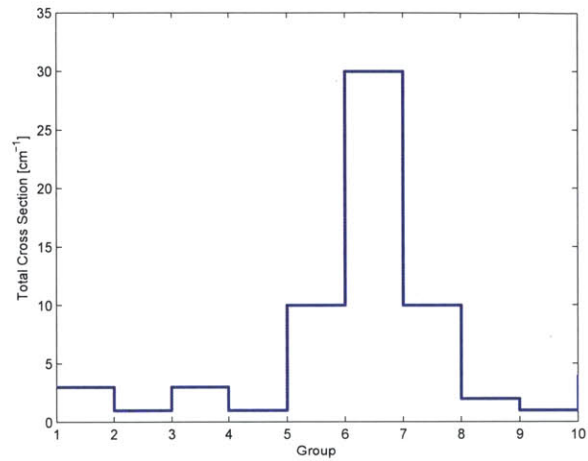


Figure 3.6: Total cross section for 10 group example problem

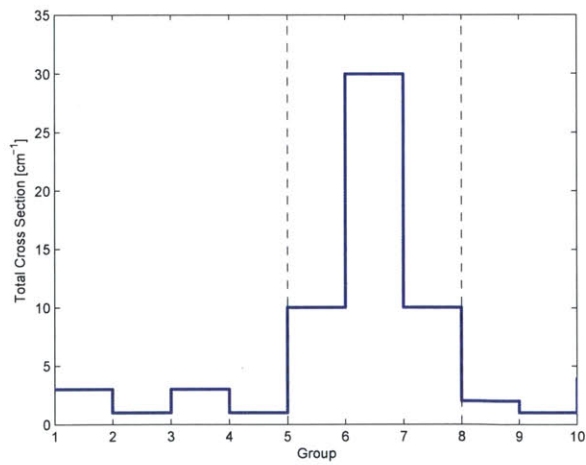
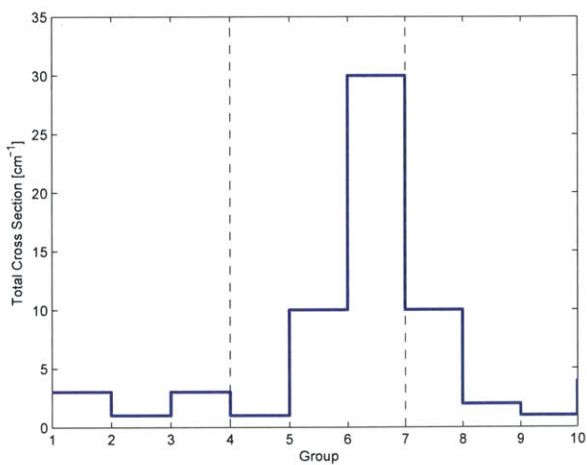


Figure 3.7: Poor choice of group map (left); Good choice of group map (right)

they are generated with either a recursion relation or directly with a Rodrigues formula. However, with Discrete Cosine Transforms, a loss of orthogonality is not seen, as arbitrary order basis sets can be generated with simple cosine evaluations. However, there is still an optimal number of fine groups per coarse group, as increased computational expense of moment generation will eventually outweigh the savings from the reduction in groups in the eigenproblem. Thus, regardless of the basis, a group mapping algorithm should limit the number of fine groups per coarse group.

Finally, it is recognized that certain group boundaries are convenient for reasons other than stability. For instance, if one desires to generate two-group reaction rates, it is preferred to force a coarse group break at a given two-group boundary. In past work [Zhu and Forget, 2011a], it was also observed that forcing a group break at the top upscatter group is beneficial computationally for most thermal reactor problems. Forcing group breaks has not been observed to adversely affect stability, and so this can be included in any group mapping algorithm.

This leaves us with the following basic algorithm to choose a group map:

*Basic algorithm:*

1. Limit ratio of smallest to largest cross section in coarse group.
2. Relax ratio condition for coarse groups with only small cross sections.
3. Cap number of fine groups per coarse group.
4. Force coarse group breaks where desired.

Recommended limits are:

- Smallest to largest cross section ratio: 2
- Small cross section limit:  $1.5 \text{ cm}^{-1}$
- Maximum fine groups per coarse group: 60.

These limits are likely not optimal, but have been found to lead to stable DGM solutions for all problems considered with Krasnoselskij iteration with  $\lambda = 0.7$ . Both the ratio and small cross section limits were attempted to be maximized while still assuring stability. The maximum number of coarse groups was less rigorously selected as an attempt to balance moment generation expense with savings from the smaller eigenproblem.

It should be noted that these limits are certainly problem dependent. A set of limits that works for all problems is undoubtedly overly conservative for certain problems. Also, the limits could be adjusted to allow other values of  $\lambda$  to be stable, including Picard iteration; however, there is little motivation for this at this time. The balance required for determining the maximum fine groups per coarse group is a function of many variables including the number of unknowns, the dominance ratio, *etc.*

Finally, it is recognized that more research is needed for this algorithm to be optimal. For instance, it is likely that considering cross sections other than the total could yield a better algorithm. Likewise, basing the group map on reaction rates instead of cross section may be much more effective; however, this also makes the map dependent upon the flux and so would vary at each recondensation step.

Now, the example problem of an infinite medium comprised of a UO<sub>2</sub>-water mixture with the SLEM-361 group structure is revisited with this group mapping algorithm. Consider the two group maps, shown in Fig. 3.8 and Fig. 3.9.

The first arbitrarily sets 9 fine groups per coarse group, resulting in 40 coarse groups. In order for convergence to be achieved, Krasnoselskij iteration is needed with a maximum  $\lambda$  of 0.032. As expected with such a small value of  $\lambda$ , convergence is extremely slow, requiring 404 iterations.

The second map uses the proposed group map algorithm with recommended limits. This also leads to a coarse group structure of 40 coarse groups. In this map, group boundaries are concentrated near the major resonances. In non-resonant fine groups, much larger coarse groups are observed. Krasnoselskij iteration is convergent for all values of  $\lambda$ , including the case of Picard iteration or  $\lambda = 1$ . Only 49 iterations are required for the same level of convergence.

It is clear that an informed choice of group map is a necessity for the DGM method. As cases with more groups are considered, it is expected that the ratio of fine groups to coarse groups will decrease. With more groups, resonances are better resolved, leading to lesser disparity in neighboring groups. Furthermore, in non-resonant energy regimes, many more coarse groups with large numbers of fine groups can be expected.

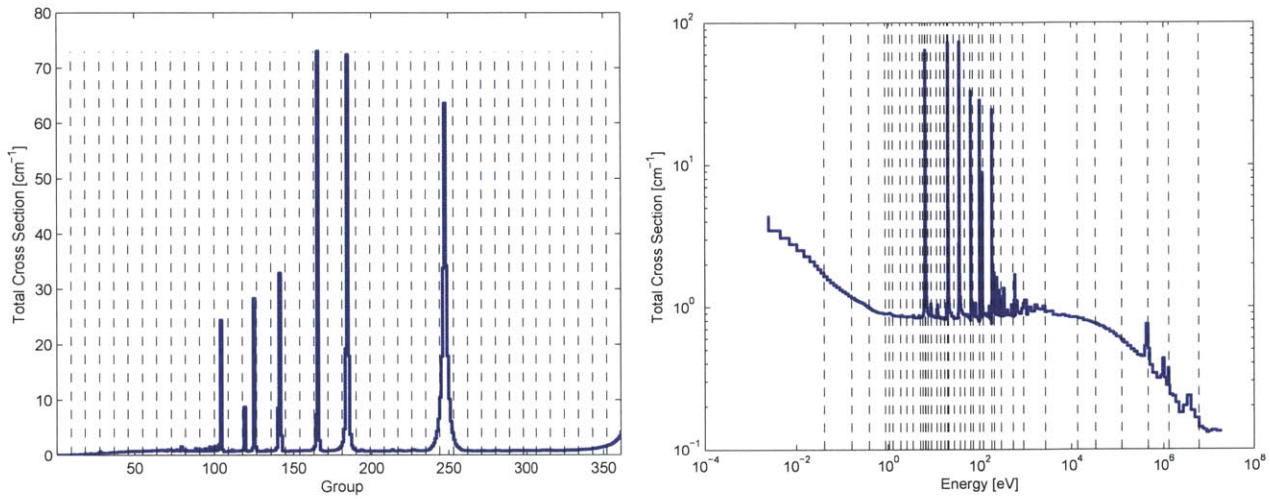


Figure 3.8: Poor choice of group map, 9 fine groups per coarse group

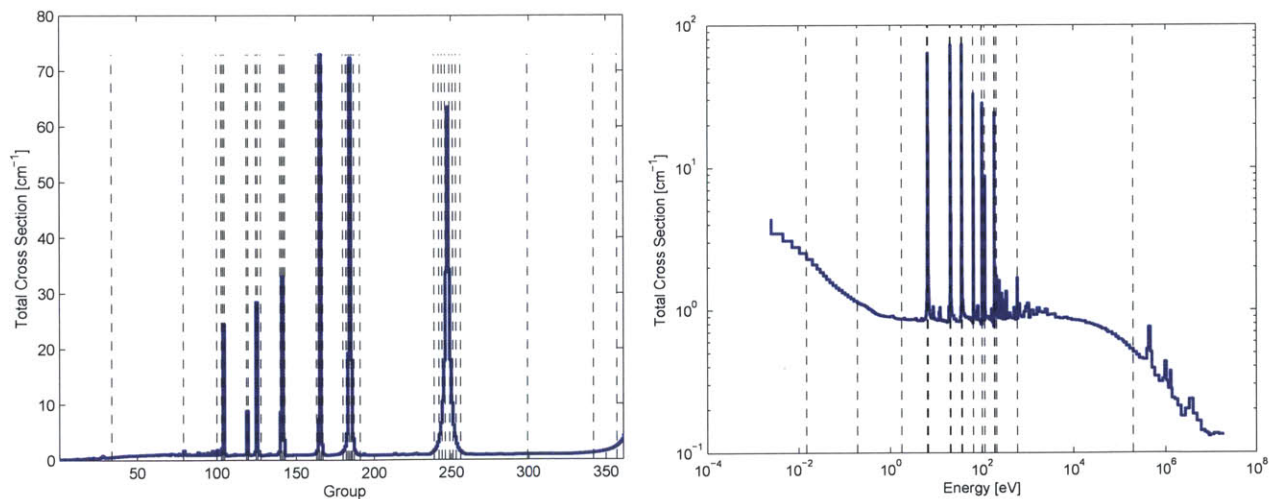


Figure 3.9: Good choice of group map, coarse group boundaries at jumps in cross section

# **Chapter 4**

## **Computational Results**

### **4.1 BWR Core Benchmark**

#### **4.1.1 Problem Description**

A 1-D computational benchmark problem is used to demonstrate the methods developed in Ch. 3. The benchmark is adapted from the benchmark problem presented by Rahnema et al. [2008]. BWR reactors are modeled in slab geometry with a series of seven assemblies. Each assembly is made up of two half slabs of water surrounding four fuel slabs. These cores represent both supercritical and subcritical systems, varying amounts of highly absorbing materials present (as gadolinium mixed in with the fuel), and different fissile materials. The geometry is shown in Fig. 4.1.

Each fuel slab is 3.2512 cm in width; each water half slab is 1.1176 cm in width. Thus, each assembly is 15.24 cm and the full core is 106.68 cm in width. Cores 1, 2, and 3, are taken from reference. Core 1 features two enrichments of  $\text{UO}_2$ . Core 2 features a small amount of gadolinium in alternating assemblies. Core 3 replaces the gadded assemblies from Core 2 with more heavily gadded assemblies. Core 4, introduced for this study, alternates between  $\text{UO}_2$  and MOX fueled assemblies. Fuel 1 is a low enriched fuel, with approximately 2% U-235. Fuel 2 is a higher enrichment, with approximately 4% U-235. The MOX fuel is approximately 90% uranium with the higher enrichment and 10% minor actinides, defined in Tab. 2.3. Table 4.1 gives the isotopic compositions of each of the materials in the benchmark problem.

Solutions are obtained using the discrete ordinates method. A 10-point Gauss-Legendre quadrature is used. Only isotropic scattering is considered. The step difference spatial discretization is used. The  $S_{10}$  solver, used both for a reference and in the DGM equations, is unaccelerated. A uniform mesh spacing of 0.4 cm is used. Two energy group structures are considered, SLEM361 and NG2042. All calculations were performed in a Fortran 2003 implemenation and run on a desktop computer with

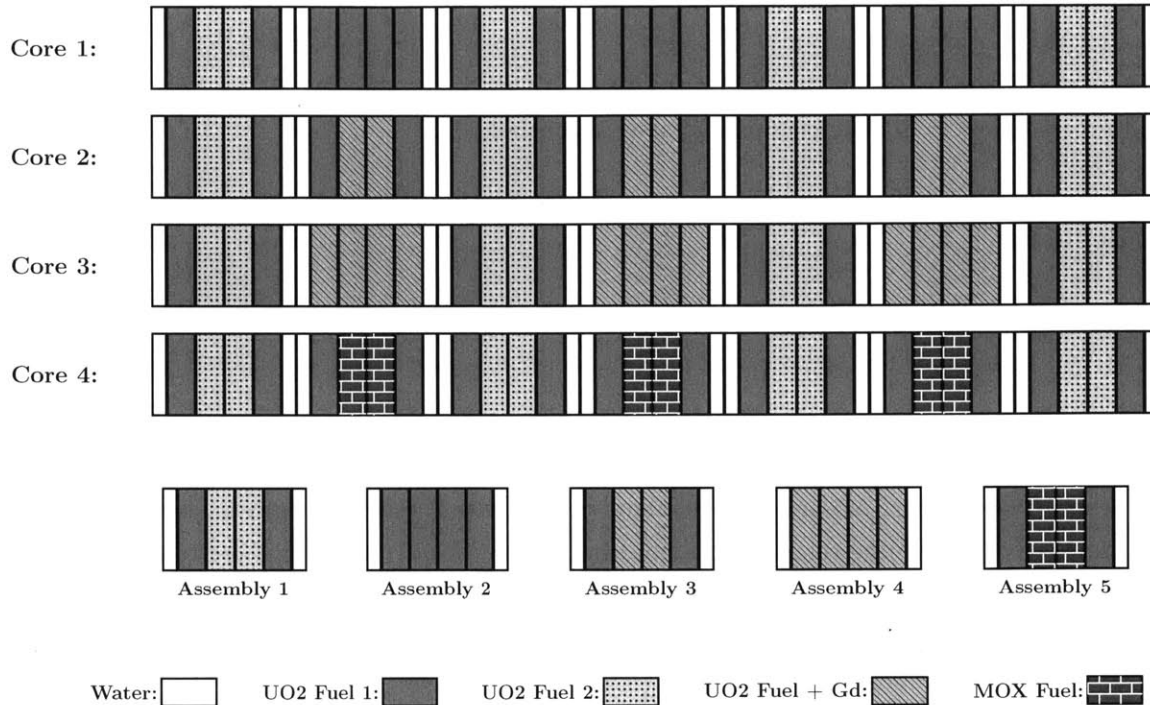


Figure 4.1: Geometry of 1-D BWR benchmark problem

Table 4.1: Isotopic compositions of materials in 1-D BWR benchmark problem

Isotope	Concentration [a/b·cm]				
	Water	UO <sub>2</sub> Fuel 1	UO <sub>2</sub> Fuel 2	UO <sub>2</sub> Fuel 2 + Gd	MOX Fuel
H-1	4.03E-2	2.73E-2	2.73E-2	2.73E-2	2.73E-2
O-16	2.02E-2	2.87E-2	2.87E-2	2.86E-2	2.86E-2
Zr-0	7.86E-3	4.79E-3	4.79E-3	4.79E-3	4.79E-3
U-234	-	1.50E-6	2.52E-6	2.63E-6	2.32E-6
U-235	-	1.68E-4	2.75E-4	2.87E-4	2.53E-4
U-238	-	7.39E-3	7.28E-3	6.88E-3	6.70E-3
Gd-154	-	-	-	9.68E-6	-
Gd-155	-	-	-	6.58E-5	-
Gd-156	-	-	-	9.10E-5	-
Gd-157	-	-	-	6.96E-5	-
Gd-158	-	-	-	1.10E-4	-
Gd-160	-	-	-	9.80E-5	-
Np-237	-	-	-	-	3.23E-5
Pu-238	-	-	-	-	1.59E-5
Pu-239	-	-	-	-	2.93E-4
Pu-240	-	-	-	-	1.32E-4
Pu-241	-	-	-	-	6.38E-5
Pu-242	-	-	-	-	3.76E-5
Am-241	-	-	-	-	2.04E-5
Am-242	-	-	-	-	1.05E-5

an Intel i7-870 CPU @ 2.93 GHz. DGM solutions use Krasnoselskij iteration with varying choices of  $\lambda$ . The group mapping algorithm is used with the recommended limits from Sec. 3.2.3. Reference solutions are taken to be direct fine group solutions. In all cases, starting guesses for the fluxes are constant group fluxes in all fine groups and spatial meshes.

### 4.1.2 Results

#### Search for Optimal $\lambda$

Cores 2 and 4 were solved with several values of  $\lambda$ . Table 4.2 gives the summary of group maps used for these problems. Figure 4.2 and Fig. 4.3 show results with the SHEM361 group structure for Cores 2 and 4, respectively. Figure 4.4 and Fig. 4.5 show results with the NG2042 group structure for Cores 2 and 4, respectively. Similar results were obtained with Cores 1 and 3, but are omitted from this thesis.

In all cases, the optimal value of  $\lambda$  was found to correspond to the maximum stable value. For both cores with the SHEM361 group structure, the maximum stable value of  $\lambda$  is approximately 0.8. With the NG2042 group structure, clear instabilities are not seen, but the convergence behavior is not as smooth as desired with  $\lambda = 1$ . Thus, the maximum stable value of  $\lambda$  can be considered to be approximately 0.9.

Note, though, that the instabilities set in after the initial improvement in reaction rates from the first few iterations. The value of  $\lambda$  could be reduced after the first few iterations to gain the faster early convergence but avoid the instabilities. This would be a shift from Krasnoselskij iteration to Mann iteration. However, the  $\lambda$  trajectory must be determined *a priori* if there is to be any benefit. Any algorithm to observe the oscillatory behavior characteristic of instability and adjust  $\lambda$  accordingly would be outperformed by an initially stable choice of  $\lambda$ .

Also in all cases, the convergence behavior is seen to exhibit a shoulder. That is, reaction rate errors decrease quickly for the first several iterations, but ultimately reach a slower asymptotic convergence rate. Because the desired use of the recondensation procedure is to improve reaction rates with only a few recondensation steps, slow asymptotic convergence is not a concern.

Note that the number of iterations to achieve convergence decreases significantly when moving from the SHEM361 group structure to the NG2042 group structure. This can be explained by considering

Table 4.2: Fine-to-coarse group maps for BWR benchmark calculations

Structure	Core 2	Core 4
SHEM361	361 → 40	361 → 46
NG2042	2042 → 86	2042 → 89

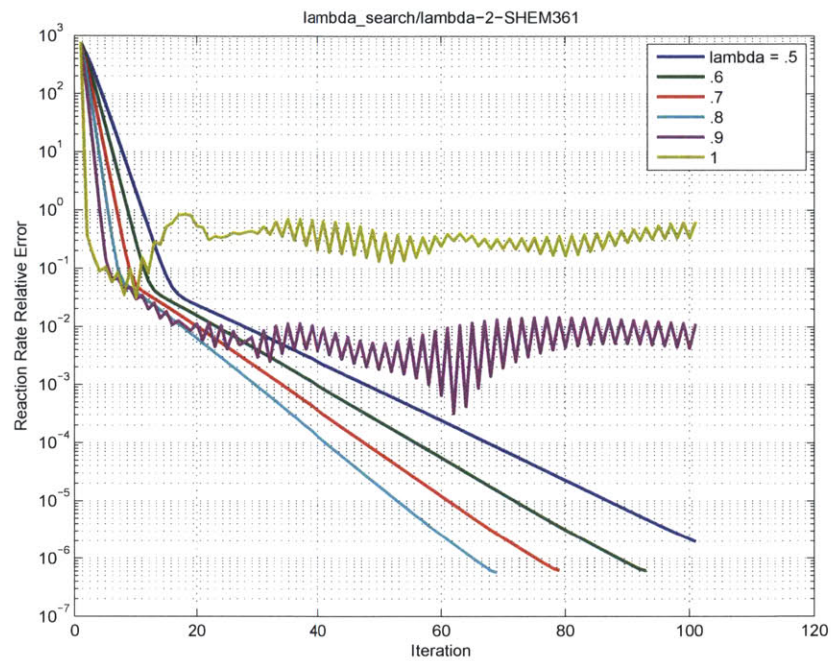


Figure 4.2: Core 2 reaction rate errors, SHEM361 group structure

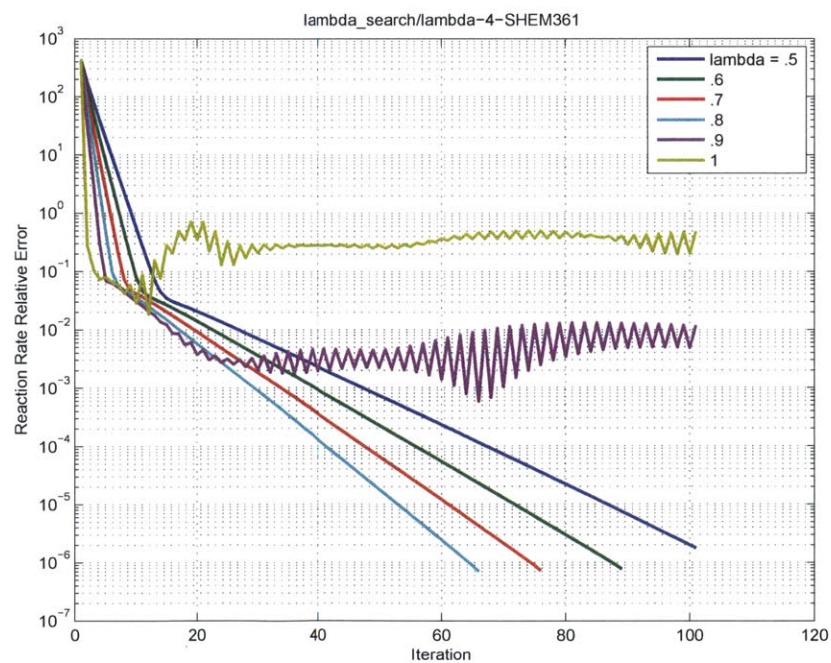


Figure 4.3: Core 4 reaction rate errors, SHEM361 group structure

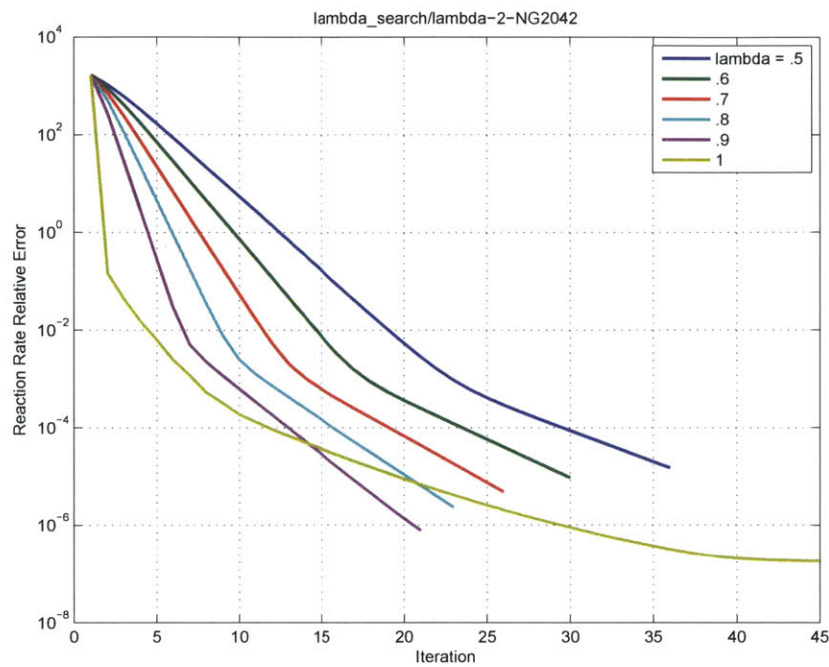


Figure 4.4: Core 2 reaction rate errors, NG2042 group structure

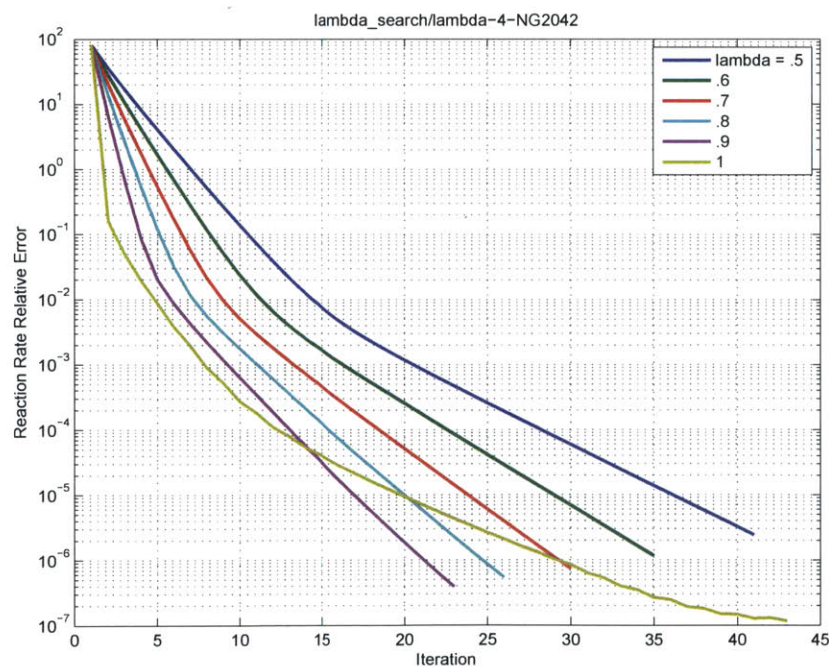


Figure 4.5: Core 4 reaction rate errors, NG2042 group structure

the fine group structures. The SHEM361 group structure contains very disparate cross sections in neighboring groups, as it represents the resonance structure with very few groups. Thus, the solution is very dependent upon the fine group detail, and the map to a coarse group structure struggles to pick up the spectral effects. For the NG2042 group structure, resonances are represented with many more groups, leading to smoother cross sections. Thus, the influence of the higher order solutions is reduced, and the coarse group solution better represents the true solution.

### Comparison to Power Iteration

Convergence behavior and timing results for Cores 2 and 4 are compared to power iteration. As before, similar results were obtained for Cores 1 and 3 but are omitted. DGM calculations used Krasnoselskij iteration with the maximum stable  $\lambda$  as determined previously and also with a lesser value of  $\lambda$ . Convergence for these comparisons is defined as the  $L_2$ -norm of coarse group reaction rate differences of successive iterates dropping below  $10^{-6}$ .

Table 4.3 gives timing comparisons for the SHEM361 group structure. Figure 4.6 and Fig. 4.7 give plots of the reaction rate errors for Cores 2 and 4, respectively, with  $\lambda = 0.8$ . The dotted lines give the  $L_2$ -norm of the difference between coarse group reaction rates at successive iterations, whereas the solid lines give the  $L_2$ -norm of reaction rate errors, compared to the fully converged solution. Note that the nonphysical shapes of the curves that are present for the last few iterations are due to limited accuracy of the reference solution. Also note that iteration counts in this context are not directly comparable. A DGM iteration represents a full recondensation step, including a fully converged power iteration solution on the coarse group. The power iterations are single fine group fixed source solutions, connected by the standard power iteration procedure.

A drastic improvement in reaction rate errors is seen in the DGM iteration after the first few iterations. However, power iteration has less error after its first iteration than DGM has after several iterations. The rate of convergence with respect to DGM recondensation steps and to fine group power iterations are approximately equal for a large portion of the results. In terms of computational time, power iteration far outperforms DGM for full convergence.

Note that in this case, the DGM solution can be accelerated by performing a single power iteration before beginning the DGM procedure. This allows the computational time associated with the DGM

Table 4.3: Timing results for benchmark problem with SHEM361 group structure

Method	Time [s]	
	Core 2	Core 4
Power Iteration	337	379
DGM ( $\lambda = 0.8$ )	1202	1027
DGM ( $\lambda = 0.7$ )	1626	1497

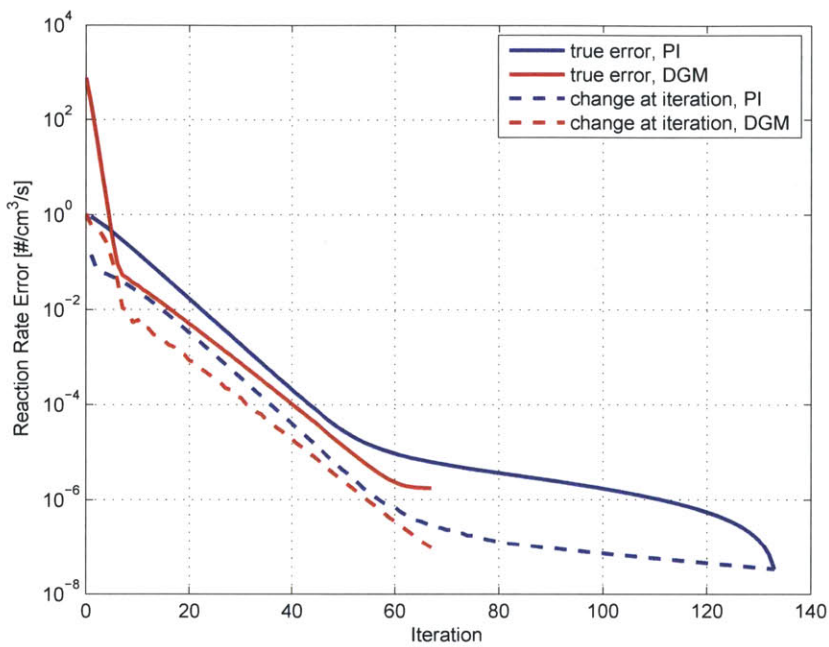


Figure 4.6: Reaction rate errors, Core 2,  $\lambda = 0.8$ , SHEM361 group structure

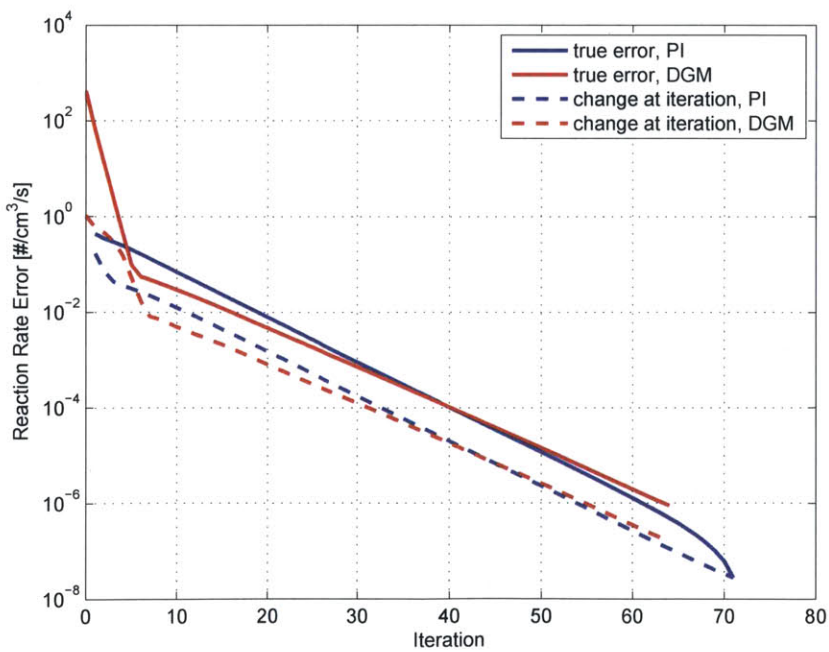


Figure 4.7: Reaction rate errors, Core 4,  $\lambda = 0.8$ , SHEM361 group structure

solution to be approximately the same as the power iteration results. By alternating between power iterations and DGM recondensation steps, full convergence can be accelerated. This observation was not studied in detail, as accelerating the fine group solution is not the goal of this study. However, this suggests that DGM can be used to accelerate power iteration in some cases. Similar work was previously performed by Zhu and Forget [2011b].

Table 4.4 gives timing comparisons for the NG2042 group structure. Figure 4.8 and Fig. 4.9 give plots of the reaction rate errors for Cores 2 and 4, respectively, with  $\lambda = 0.9$ . As in the previous plots, the dotted lines give the  $L_2$ -norm of the difference between coarse group reaction rates at successive iterations, whereas the solid lines give the  $L_2$ -norm of the reaction rate errors, compared to the fully converged solution. Again, nonphysical shapes of the curves at the last few iterations are due to the limited accuracy of the reference solution.

Table 4.4: Timing results for benchmark problem with NG2042 group structure

Method	Time [s]	
	Core 2	Core 4
Power Iteration	24530	18300
DGM ( $\lambda = 0.9$ )	2820	2667
DGM ( $\lambda = 0.8$ )	3205	2889

For this finer group structure, DGM far outperforms direct fine group power iteration. The fully converged DGM solution requires less time than a single fine group power iteration. Also, as shown previously, results with the NG2042 group structure require fewer DGM steps to obtain convergence compared to those with the SHEM361 structure. The convergence rate of the DGM solution with respect to recondensation steps is considerably greater than that of fine group power iteration.

Note that some of the discrepancy in times can be attributed to the unaccelerated nature of the non-performance-oriented implementation used to create these results. Performance comparisons using the DETRAN discrete ordinates code under development at MIT [Roberts, 2012] showed that a performance-oriented implementation greatly reduces the cost of the transport calculation. This issue was not seen with the SHEM361, which suggests that cache management is likely the issue at play. Using the Krylov solvers implemented in DETRAN allowed the fine group solution to be accelerated to approximately the computational expense of the unaccelerated DGM solution.

## 4.2 Ultrafine Pin-Cell Results

Due to the large computational time and memory requirements of an ultrafine solution of the 1-D BWR benchmark problems, a different benchmark problem was used to evaluate the algorithmic changes for an ultrafine group representation. Thus, the pin-cell problem considered in Sec. 2.2.2 is

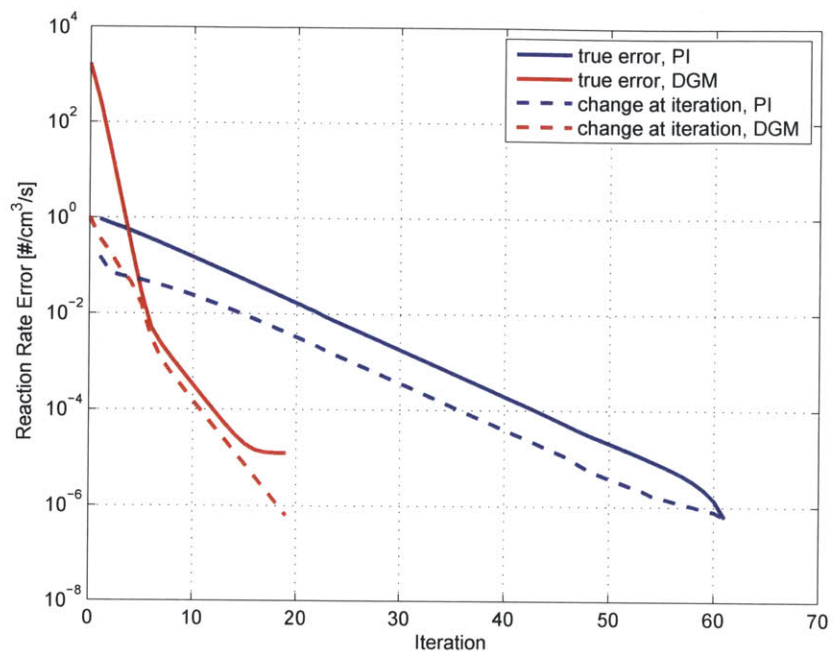


Figure 4.8: Reaction rate errors, Core 2,  $\lambda = 0.9$ , NG2042 group structure

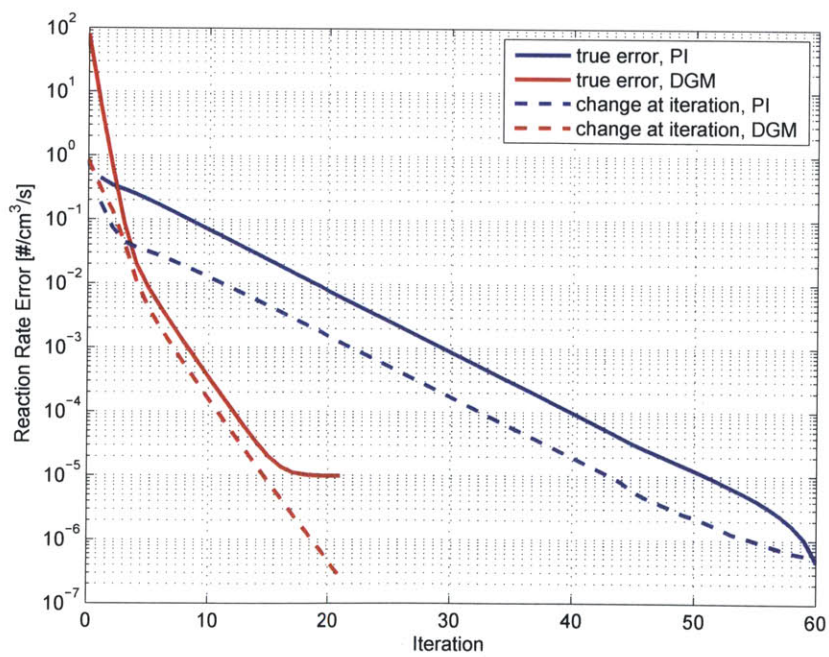


Figure 4.9: Reaction rate errors, Core 4,  $\lambda = 0.9$ , NG2042 group structure

revisited. The geometry is given in Fig. 2.2, and the material concentrations are given in Tab. 2.10. The width of the  $\text{UO}_2$  slab is 0.393 cm; the width of the water slab is 0.238 cm.

Four mesh points in each slab were used. The group mapping algorithm with recommended limits from Sec. 3.2.3 were used, which resulted in a  $14767 \rightarrow 600$  group mapping. Krasnoselskij iteration with  $\lambda = 0.7$  was used for this case, and is likely considerably below the optimal value. Table 4.5 gives the eigenvalue error for the first several iterations for this problem. The reference eigenvalue, taken as a fully converged solution, is 1.255293.

Table 4.5: UF14767 pin-cell problem results

Iteration	$k$	$k$ Error [pcm]
1	1.24289	1241
2	1.24693	837
3	1.25132	398
4	1.25399	131
5	1.25492	38
6	1.25520	9
7	1.25529	0.4

Table 4.6 gives a timing summary of the first few DGM iterations for this problem. Moment generation dominates the time spent at each generation, with the majority of the expense being in computing moments for the scattering matrix. This is clearly the bottleneck in the algorithm now and will be the subject of future work. The coarse group transport equation solution and the solution of the higher order equations are essentially computationally free compared to the moment generation.

Table 4.6: Timing summary of first few DGM iterations for pin-cell problem with UF14767 group structure. Steps include moment generation, solving the coarse group transport equation, and solving the higher order equations.

Iteration	Time [s]		
	Moments	Coarse TE	HO Eqns
1	225	1.5	2.0
2	226	1.5	2.0
3	225	1.7	2.0

Comparing these results to Tab. 2.12, which solved the same problem with flux updates, the significance of the results are easily seen. The elimination of flux updates greatly reduced the computational time associated at each time step. The discrepancies in time in the other phases of the recondensation procedure can be attributed to the different group map used. With the group mapping algorithm, considerably more coarse groups were found to be required. This shifts some of the computational expense associated with moment generation and the higher order equations to the coarse group solution. Because of the enormous computational expense associated with moment generation, there is little desire to use less groups at the coarse group level at this time.

## **Chapter 5**

# **Conclusions and Future Work**

### **5.1 Conclusions**

Although today's light water reactors are modeled with sufficient accuracy for design and operational purposes, classical reactor physics methodologies are not able to adapt to tomorrow's applications. In the near term, alternate reactor materials, such as silicon carbide cladding and uranium nitride fuel, are being proposed for use in light water reactors. Recycled plutonium and transuramics are already being used in some reactors as mixed oxide fuels. In the longer term, new reactor designs—such as sodium cooled fast reactors, graphite moderated high temperature reactors, and molten salt reactors—provide even more challenges for today's simulations.

One means of addressing these challenges is to forgo self-shielding approximations in favor of using continuous energy or ultrafine multigroup nuclear data to fully resolve the complexities in energy space. Because this is associated with a high computational cost—both in computational time and memory requirements—a means of approximating a solution of this fidelity without the associated expense is desired. The Discrete Generalized Multigroup (DGM) method is proposed to be a possible means of accomplishing this.

This study examined the feasibility of using the DGM method with an ultrafine energy mesh to treat resonance self-shielding phenomena. Infinite medium and simple 1-D calculations were performed to identify obstacles associated with this procedure. Four such obstacles were identified:

1. The UF14767 ultrafine energy mesh is not sufficient to fully resolve resonance effects for all problems.
2. Memory requirements associated with an explicit scattering matrix in the ultrafine framework are enormous.

3. Computational expense of computing DGM moments becomes very large as the number of groups used grows.
4. Flux updates used for stability are prohibitively expensive.

As this was only a feasibility study, the lacking performance of the UF14767 library was not a concern. One can simply increase the number of groups, shifting this obstacle to additional memory and computational expense. Before a production level implementation of this method could be made, the energy mesh needs to be studied and optimized. However, the results of this study would not be significantly impacted by moving to a different energy mesh.

Both the large memory requirements and computational time associated with storing and computing moments for an explicit scattering matrix is an open problem with the method, and is discussed in more detail as future work in Sec. 5.2.1.

The need for flux updates to maintain stability of the algorithm was removed through the introduction of Krasnoselskij iteration and a group mapping algorithm. Krasnoselskij iteration relaxes the fixed point iteration procedure, allowing the scheme to converge without flux updates with an appropriate choice of the characteristic parameter  $\lambda$ . This alone is not enough to make the the algorithm attractive, however, as the small value of  $\lambda$  required for an arbitrary group map to be convergent leads to a very large number of iterations being required for reasonable accuracy to be achieved.

The impact of the fine to coarse group map on stability was then investigated. It was found that instabilities arise due to large disparities in cross sections inside a coarse group. Thus, if group boundaries are set at large jumps in cross section, greatly improved stability can be obtained. This was shown to be very successful at maintaining stability in the recondensation procedure and still allows good accuracy to be obtained in relatively few iterations.

The improved recondensation procedure developed here were shown to be successful on a 1-D BWR benchmark problem with the SHEM361 and NG2042 group structures and on a simple 1-D pin-cell with the UF14767 group structure. Starting from a constant guessed flux, reaction rate errors dropped below 0.1% in 30 recondensation steps with SHEM361 and within 10 recondensation steps with NG2042. The eigenvalue error dropped below 50 pcm after only 5 recondensation iterations on the pin-cell problem with UF14767. Furthermore, the UF14767 pin-cell required less than half the computational time per recondensation step than without the improved procedure.

With relatively few iterations needed for sufficient accuracy, faster convergence for larger number of groups, and improved stability characteristics, the improved recondensation procedure for the DGM method is an attractive option for ultrafine multigroup simulations.

## 5.2 Future Work

### 5.2.1 Scattering Kernel Representation

The primary obstacle associated with a production level implementation of DGM to model resonance self-shielding phenomena is the scattering matrix. In this study, a fully explicit scattering matrix was used and was shown to be a large computational burden, both in computational time and memory requirements. Many options exist to approximate the scattering kernel to alleviate this burden.

As discussed in Sec. 1.3.1, many approximations to the scattering kernel are currently employed in existing uses of ultrafine energy meshes. These include assuming a simple  $1/E$  shape of the scattering source throughout the resonance region, modeling the inelastic scattering at a coarse group level and computing the elastic scattering kernel on the fly, using a dual energy resolution, and using a submoment approximation.

The DGM framework provides another possible representation. The scattering kernel can be represented in fewer groups than the transport kernel is modeled. If a consistent two-part group map is used, the scattering and transport kernels could communicate at the coarse group level without complication. The higher order equations would not all have scattering sources in them.

### 5.2.2 Lattice Physics Implementation

The ultimate goal of this research is to provide a lattice physics methodology that does not rely on crude self-shielding approximations. A DGM recondensation procedure could be implemented at the lattice level with an ultrafine energy mesh to realize this goal.

Because the spatial complexity in a typical lattice physics calculation exceeds that studied in this thesis, this requires an efficient DGM implementation in order to make the problem tractable. In addition to reducing the expense associated with the scattering kernel, anisotropic scattering must also be considered.

Also, in order to fully capture the physics, a validated ultrafine energy mesh must be employed. This may involve introducing additional groups to the UF14767 group library or, alternatively, performing a group boundary optimization process. However, it is imperative that the resultant group structure be applicable to all potential problems and not be specific to only certain classes of problems.

# References

- Aggery, A. (1999). Calculs de référence avec un maillage multigroupe fin sur des assemblages critiques par APOLLO 2. Technical Report CEA-N-2848, Commissariat à l'Energie Atomique – France. (French).
- Ahmed, N., Natarajan, T., and Rao, K. R. (1974). Discrete cosine transform. *IEEE Transactions on Computers*, pages 90–93.
- Bell, G. I. and Glasstone, S. (1970). *Nuclear Reactor Theory*. Van Nostrand Reinhold Company.
- Berinde, V. (2004). *Iterative Approximation of Fixed Points*, volume 1912 of *Lecture Notes in Mathematics*. Springer, second edition.
- Cullen, D. E. (2010). *Nuclear Data Preparation*, volume 1 of *Handbook of Nuclear Engineering*, pages 279–425. Springer.
- Douglass, S. and Rahnema, F. (2011). Cross section recondensation method via generalized energy condensation theory. *Annals of Nuclear Energy*, 38:2105–2110.
- Douglass, S. and Rahnema, F. (2012a). Consistent generalized energy condensation theory. *Annals of Nuclear Energy*, 40:200–214.
- Douglass, S. and Rahnema, F. (2012b). Subgroup decomposition method. *Annals of Nuclear Energy*, 48:84–101.
- Duderstadt, J. J. and Hamilton, L. J. (1976). *Nuclear Reactor Analysis*. John Wiley & Sons.
- Forget, B. and Rahnema, F. (2007). A spectral unfolding method.
- Gibson, N. A. and Forget, B. (2012a). Application of the discrete generalized multigroup method to ultra-fine energy mesh in infinite medium calculations. *PHYSOR 2012 – Advances in Reactor Physics Linking Research, Industry, and Education*.
- Gibson, N. A. and Forget, B. (2012b). Eliminating flux updates from the discrete generalized multi-group method. *Transactions of the American Nuclear Society*.

- Hébert, A. (2009). *Applied Reactor Physics*. Presses Internationales Polytechnique.
- Hébert, A. and Santamarina, A. (2008). Refinement of the Santamarina-Hfaiedh energy mesh between 22.5 eV and 11.4 keV. *International Conference on Reactor Physics, Nuclear Power: A Sustainable Resource*.
- Hfaiedh, N. and Santamarina, A. (2005). Determination of the optimized SHEM mesh for neutron transport calculations. *Mathematics and Computation, Supercomputing, Reactor Physics and Nuclear and Biological Applications*.
- Huria, H. and Ouisloumen, M. (2008). An optimized ultra-fine energy group structure for neutron transport calculations. *International Conference on the Physics of Reactors – Nuclear Power: A Sustainable Resource*.
- Krasnoselskij, M. A. (1955). Two remarks on the method of successive approximations. *Uspehi Mat. Nauk.*, 10(1/63):123–127. (Russian).
- Kucukboyaci, V. N., Ouisloumen, M., and Franceschini, F. (2009). Two-dimensional whole core transport calculations using PARAGON. *International Conference on Mathematics, Computational Methods & Reactor Physics (M&C 2009)*.
- Lathrop, K. D. and Carlson, B. G. (1964). Discrete ordinates angular quadrature of the neutron transport equation. Technical Report LA-3186, Los Alamos National Laboratory.
- Lewis, E. E. and Miller, W. F., J. (1993). *Computational Methods of Neutron Transport*. American Nuclear Society.
- Macfarlane, R. E. (2000). *PSR-480/NJOY99.0: Code System for Producing Pointwise and Multigroup Neutron and Photon Cross Sections from ENDF/B Data*. Los Alamos National Laboratory.
- Mosteller, R. D., Eisenhart, L. D., Little, R. C., Eich, W. J., and Chao, J. (1991). Benchmark calculations for the doppler coefficient of reactivity. *Nuclear Science and Engineering*, 107:265–271.
- Neuman, C. P. and Schonbach, D. I. (1974). Discrete (Legendre) orthogonal polynomials—a survey. *International Journal for Numerical Methods in Engineering*, 8:743–770.
- Rahnema, F., Douglass, S., and Forget, B. (2008). Generalized energy condensation theory. *Nuclear Science and Engineering*, 160:41–58.
- Reuss, P. (2008). *Neutron Physics*. EDP Sciences.
- Roberts, J. A. (2012). *libdetran: Deterministic Transport Utilities*. Massachusetts Institute of Technology. <http://github.com/robertsj/libdetran>.
- Romano, P. K. and Forget, B. (2013). The OpenMC Monte Carlo particle transport code. *Annals of Nuclear Energy*, 51:274–281.

- Stacey, W. M. (2007). *Nuclear Reactor Physics*. Wiley-VCH, second edition.
- Sugimura, N. and Yamamoto, A. (2007). Resonance treatment based on ultra-fine-group spectrum calculation in the AEGIS code. *Journal of Nuclear Science and Technology*, 44(7):958–966.
- van Rooijen, W. F. G. (2012). Feasibility of wavelet expansion methods to treat the energy variable. *PHYSOR 2012 – Advances in Reactor Physics Linking Research, Industry, and Education*.
- Williams, M. L. and Asgari, M. (1995). Computation of continuous energy neutron spectra with discrete ordinates transport theory. *Nuclear Science and Engineering*, 121:173.
- Yamamoto, A., Endo, T., Tabuchi, M., Sugimura, N., Ushio, T., Mori, M., Tatsumi, M., and Ohoka, Y. (2010). AEGIS: An advanced lattice physics code for light water reactor analyses. *Nuclear Engineering and Technology*, 42(5):500–519.
- Zerkle, M. L., Abu-Shumays, I. K., Ott, M. W., and Winwood, J. P. (1997). Theory and application of the RAZOR two-dimensional continuous energy lattice physics code. Technical Report WAPD-T-3156, Bettis Atomic Power Laboratory.
- Zhu, L. (2012). *Discrete Generalized Multigroup Theory and Applications*. PhD thesis, Massachusetts Institute of Technology.
- Zhu, L. and Forget, B. (2010). A discrete generalized multigroup energy expansion theory. *Nuclear Science and Engineering*, 166:239–253.
- Zhu, L. and Forget, B. (2011a). An energy recondensation method using the discrete generalized multigroup energy expansion theory. *Annals of Nuclear Energy*, 38:1718–1727.
- Zhu, L. and Forget, B. (2011b). A nonlinear acceleration method. *Transactions of the American Nuclear Society*.

## Appendix A

### TRESFIN Thermal Block

The 525 energy bounds defining the TRESFIN thermal block are given here.

Energy Group Boundaries [eV]				
1.1000000e-04	5.0000000e-04	8.0000000e-04	1.0000000e-03	1.3000000e-03
1.7000000e-03	2.3000000e-03	3.0000000e-03	3.5000000e-03	4.0000000e-03
4.5000000e-03	5.0000000e-03	5.5000000e-03	6.0000000e-03	6.5000000e-03
6.9000000e-03	7.9340000e-03	8.9670000e-03	1.0000000e-02	1.1250000e-02
1.2500000e-02	1.3750000e-02	1.5000000e-02	1.6250000e-02	1.7500000e-02
1.8750000e-02	2.0000000e-02	2.1250000e-02	2.2500000e-02	2.3750000e-02
2.5000000e-02	2.6250000e-02	2.7500000e-02	2.8750000e-02	3.0000000e-02
3.1250000e-02	3.2500000e-02	3.3750000e-02	3.5000000e-02	3.6750000e-02
3.8500000e-02	4.0250000e-02	4.2000000e-02	4.4000000e-02	4.6000000e-02
4.8000000e-02	5.0000000e-02	5.2000000e-02	5.4000000e-02	5.6000000e-02
5.8000000e-02	6.0250000e-02	6.2500000e-02	6.4750000e-02	6.7000000e-02
6.9500000e-02	7.2000000e-02	7.4500000e-02	7.7000000e-02	8.0000000e-02
8.3750000e-02	8.7500000e-02	9.1250000e-02	9.5000000e-02	9.7500000e-02
1.0000000e-01	1.0375000e-01	1.0750000e-01	1.1125000e-01	1.1500000e-01
1.1880000e-01	1.2260000e-01	1.2640000e-01	1.3020000e-01	1.3400000e-01
1.3600000e-01	1.3800000e-01	1.4000000e-01	1.4212300e-01	1.4424700e-01
1.4637000e-01	1.4859000e-01	1.5081000e-01	1.5303000e-01	1.5535300e-01
1.5767700e-01	1.6000000e-01	1.6242800e-01	1.6485500e-01	1.6728300e-01
1.6971000e-01	1.7228300e-01	1.7485500e-01	1.7742800e-01	1.8000000e-01
1.8225000e-01	1.8450000e-01	1.8675000e-01	1.8900000e-01	1.9145300e-01
1.9390500e-01	1.9635800e-01	1.9881000e-01	2.0139200e-01	2.0397500e-01
2.0655700e-01	2.0914000e-01	2.1185500e-01	2.1457000e-01	2.1728500e-01
2.2000000e-01	2.2339500e-01	2.2679000e-01	2.3018500e-01	2.3358000e-01
2.3718500e-01	2.4079000e-01	2.4439500e-01	2.4800000e-01	2.5187800e-01
2.5575500e-01	2.5963300e-01	2.6351000e-01	2.6763300e-01	2.7175500e-01
2.7587700e-01	2.8000000e-01	2.8500000e-01	2.9000000e-01	2.9500000e-01
3.0000000e-01	3.0362500e-01	3.0725000e-01	3.1087500e-01	3.1450000e-01

3.1725000e-01	3.2000000e-01	3.2366500e-01	3.2733000e-01	3.3099500e-01
3.3466000e-01	3.3849500e-01	3.4233000e-01	3.4616500e-01	3.5000000e-01
3.5498300e-01	3.5996500e-01	3.6494800e-01	3.6993000e-01	3.7519800e-01
3.8046500e-01	3.8573300e-01	3.9100000e-01	3.9550000e-01	4.0000000e-01
4.0466300e-01	4.0932700e-01	4.1399000e-01	4.1874300e-01	4.2349500e-01
4.2824800e-01	4.3300000e-01	4.3717000e-01	4.4134000e-01	4.4551000e-01
4.4968000e-01	4.5401300e-01	4.5834500e-01	4.6267800e-01	4.6701000e-01
4.7150800e-01	4.7600500e-01	4.8050300e-01	4.8500000e-01	4.8875000e-01
4.9250000e-01	4.9625000e-01	5.0000000e-01	5.0490500e-01	5.0981000e-01
5.1471500e-01	5.1962000e-01	5.2360700e-01	5.2759300e-01	5.3158000e-01
5.3579000e-01	5.4000000e-01	5.4674000e-01	5.5348000e-01	5.6022000e-01
5.6676000e-01	5.7404000e-01	5.8112000e-01	5.8820000e-01	5.9528000e-01
6.0271000e-01	6.1014000e-01	6.1757000e-01	6.2500000e-01	6.3203800e-01
6.3907500e-01	6.4611300e-01	6.5315000e-01	6.6050200e-01	6.6785500e-01
6.7520700e-01	6.8256000e-01	6.9004000e-01	6.9752000e-01	7.0500000e-01
7.1413700e-01	7.2327500e-01	7.3241300e-01	7.4155000e-01	7.5116300e-01
7.6077500e-01	7.7038800e-01	7.8000000e-01	7.8500000e-01	7.9000000e-01
7.9736300e-01	8.0472500e-01	8.1208800e-01	8.1945000e-01	8.2708800e-01
8.3472500e-01	8.4236300e-01	8.5000000e-01	8.5500000e-01	8.6000000e-01
8.6547500e-01	8.7095000e-01	8.7642500e-01	8.8313900e-01	8.8985400e-01
8.9657000e-01	9.0328500e-01	9.1000000e-01	9.1500000e-01	9.2000000e-01
9.2500000e-01	9.3000000e-01	9.3500000e-01	9.4000000e-01	9.4500000e-01
9.5000000e-01	9.5550000e-01	9.6100000e-01	9.6650000e-01	9.7200000e-01
9.7666700e-01	9.8133300e-01	9.8600000e-01	9.9100000e-01	9.9600000e-01
1.0020000e+00	1.0079990e+00	1.0140000e+00	1.0200000e+00	1.0250000e+00
1.0300000e+00	1.0350000e+00	1.0400000e+00	1.0449990e+00	1.0502000e+00
1.0554000e+00	1.0605990e+00	1.0658000e+00	1.0709990e+00	1.0755000e+00
1.0800000e+00	1.0856670e+00	1.0913320e+00	1.0969990e+00	1.1013330e+00
1.1056660e+00	1.1100000e+00	1.1143320e+00	1.1186670e+00	1.1229990e+00
1.1297490e+00	1.1364990e+00	1.1432500e+00	1.1500000e+00	1.1550000e+00
1.1600000e+00	1.1650000e+00	1.1699990e+00	1.1780150e+00	1.1860290e+00
1.1940440e+00	1.2020600e+00	1.2102950e+00	1.2185300e+00	1.2267650e+00
1.2350000e+00	1.2430190e+00	1.2510400e+00	1.2590600e+00	1.2670790e+00
1.2753100e+00	1.2835400e+00	1.2917700e+00	1.2999990e+00	1.3093750e+00
1.3187490e+00	1.3281240e+00	1.3375000e+00	1.3456250e+00	1.3537490e+00
1.3618750e+00	1.3700000e+00	1.3786390e+00	1.3872800e+00	1.3959200e+00
1.4045590e+00	1.4134200e+00	1.4222790e+00	1.4311400e+00	1.4400000e+00
1.4487500e+00	1.4575000e+00	1.4662490e+00	1.4749990e+00	1.4833330e+00
1.4916670e+00	1.5000000e+00	1.5110850e+00	1.5221690e+00	1.5332550e+00
1.5443390e+00	1.5557550e+00	1.5671690e+00	1.5785850e+00	1.5899990e+00
1.5998770e+00	1.6097550e+00	1.6196330e+00	1.6295100e+00	1.6396320e+00
1.6497550e+00	1.6598780e+00	1.6699990e+00	1.6804920e+00	1.6909850e+00
1.7014770e+00	1.7119690e+00	1.7227280e+00	1.7334840e+00	1.7442430e+00
1.7549990e+00	1.7654990e+00	1.7759990e+00	1.7865000e+00	1.7970000e+00
1.8077500e+00	1.8185000e+00	1.8292490e+00	1.8399990e+00	1.8476940e+00
1.8553900e+00	1.8650800e+00	1.8747690e+00	1.8844590e+00	1.8958440e+00
1.9072290e+00	1.9186140e+00	1.9299990e+00	1.9411220e+00	1.9522450e+00
1.9633670e+00	1.9744890e+00	1.9858680e+00	1.9972450e+00	2.0086220e+00

2.0200000e+00	2.0299020e+00	2.0398040e+00	2.0497070e+00	2.0596090e+00
2.0730720e+00	2.0865360e+00	2.0999990e+00	2.1100000e+00	2.1200000e+00
2.1299990e+00	2.1438270e+00	2.1576550e+00	2.1714820e+00	2.1853090e+00
2.1994940e+00	2.2136790e+00	2.2278640e+00	2.2420490e+00	2.2566040e+00
2.2711590e+00	2.2857140e+00	2.3002690e+00	2.3152020e+00	2.3301340e+00
2.3450660e+00	2.3600000e+00	2.3711840e+00	2.3823700e+00	2.3954820e+00
2.4085970e+00	2.4217090e+00	2.4375390e+00	2.4533690e+00	2.4691990e+00
2.4850290e+00	2.5012710e+00	2.5175140e+00	2.5337570e+00	2.5499990e+00
2.5666660e+00	2.5833320e+00	2.5999990e+00	2.6148290e+00	2.6296600e+00
2.6444890e+00	2.6593200e+00	2.6744900e+00	2.6896590e+00	2.7048290e+00
2.7199990e+00	2.7359720e+00	2.7519460e+00	2.7679200e+00	2.7854380e+00
2.8029550e+00	2.8204730e+00	2.8379900e+00	2.8559490e+00	2.8739100e+00
2.8918700e+00	2.9098290e+00	2.9282450e+00	2.9466590e+00	2.9650750e+00
2.9834900e+00	3.0023730e+00	3.0212550e+00	3.0401370e+00	3.0590190e+00
3.0785970e+00	3.0981740e+00	3.1177520e+00	3.1373290e+00	3.1574050e+00
3.1774800e+00	3.1975550e+00	3.2176290e+00	3.2382220e+00	3.2588150e+00
3.2794080e+00	3.2999990e+00	3.3201880e+00	3.3403750e+00	3.3605620e+00
3.3807500e+00	3.4021440e+00	3.4235390e+00	3.4449350e+00	3.4663300e+00
3.4882680e+00	3.5102040e+00	3.5321430e+00	3.5540790e+00	3.5765710e+00
3.5990650e+00	3.6215560e+00	3.6440500e+00	3.6671120e+00	3.6901740e+00
3.7132380e+00	3.7363000e+00	3.7599450e+00	3.7835890e+00	3.8072350e+00
3.8308790e+00	3.8551240e+00	3.8793700e+00	3.9036150e+00	3.9278590e+00
3.9519000e+00	3.9759490e+00	4.0000000e+00	4.0258490e+00	4.0517000e+00
4.0775500e+00	4.1033990e+00	4.1292500e+00	4.1553820e+00	4.1815160e+00
4.2076480e+00	4.2337820e+00	4.2605760e+00	4.2873720e+00	4.3141650e+00
4.3409610e+00	4.3684340e+00	4.3959060e+00	4.4233800e+00	4.4508520e+00
4.4790200e+00	4.5071900e+00	4.5353570e+00	4.5635250e+00	4.5924070e+00
4.6212890e+00	4.6501700e+00	4.6790520e+00	4.7086660e+00	4.7382770e+00
4.7678910e+00	4.7975030e+00	4.8278660e+00	4.8582280e+00	4.8885900e+00
4.9189530e+00	4.9500840e+00	4.9812150e+00	5.0123450e+00	5.0434800e+00

## Appendix B

# SHEM Energy Mesh

The energy bounds of the groups in the SHEM361 energy mesh are given here. All energy bounds are given as the lower energy bound for the group. The upper energy bound for the first group is indicated as the lower bound of a fictitious zeroth group.

Group	Lower Bound [eV]	Group	Lower Bound [eV]	Group	Lower Bound [eV]
0	1.9640300e+07	1	1.4918230e+07	2	1.3840290e+07
3	1.1618330e+07	4	9.9999870e+06	5	9.0483630e+06
6	8.1872970e+06	7	7.4081730e+06	8	6.7031920e+06
9	6.0652990e+06	10	4.9658470e+06	11	4.0656910e+06
12	3.3287070e+06	13	2.7253140e+06	14	2.2312990e+06
15	1.9013870e+06	16	1.6365390e+06	17	1.4057680e+06
18	1.3369410e+06	19	1.2869610e+06	20	1.1620480e+06
21	1.0511490e+06	22	9.5111888e+05	23	8.6000581e+05
24	7.0651119e+05	25	5.7844250e+05	26	4.9400181e+05
27	4.5602109e+05	28	4.1250119e+05	29	3.8388350e+05
30	3.2064641e+05	31	2.6782641e+05	32	2.3005980e+05
33	1.9506620e+05	34	1.6506500e+05	35	1.4009759e+05
36	1.2277320e+05	37	1.1562350e+05	38	9.4664500e+04
39	8.2297359e+04	40	6.7379383e+04	41	5.5165570e+04
42	4.9915871e+04	43	4.0867660e+04	44	3.6978590e+04
45	3.3459609e+04	46	2.9281010e+04	47	2.7394410e+04
48	2.6100100e+04	49	2.4999080e+04	50	2.2699410e+04
51	1.8584711e+04	52	1.6200450e+04	53	1.4899670e+04
54	1.3603660e+04	55	1.1137740e+04	56	9.1188076e+03
57	7.4658481e+03	58	6.1125200e+03	59	5.0045078e+03
60	4.0973452e+03	61	3.4810681e+03	62	2.9961831e+03
63	2.7002361e+03	64	2.3972900e+03	65	2.0841040e+03
66	1.8118330e+03	67	1.5861970e+03	68	1.3435820e+03
69	1.1346670e+03	70	1.0643230e+03	71	9.8249408e+02
72	9.0968127e+02	73	8.3221790e+02	74	7.4851727e+02
75	6.7728650e+02	76	6.4683698e+02	77	6.1283423e+02

78	6.0009882e+02	79	5.9294067e+02	80	5.7714551e+02
81	5.3920422e+02	82	5.0174619e+02	83	4.5399869e+02
84	4.1909360e+02	85	3.9076032e+02	86	3.7170270e+02
87	3.5357459e+02	88	3.3532300e+02	89	3.1992749e+02
90	2.9592151e+02	91	2.8832669e+02	92	2.8488751e+02
93	2.7646780e+02	94	2.6829691e+02	95	2.5674780e+02
96	2.4179601e+02	97	2.3559030e+02	98	2.2432471e+02
99	2.1210770e+02	100	2.0095770e+02	101	1.9599600e+02
102	1.9307800e+02	103	1.9020351e+02	104	1.8887669e+02
105	1.8755920e+02	106	1.8625079e+02	107	1.8495160e+02
108	1.8329450e+02	109	1.7522910e+02	110	1.6751860e+02
111	1.6305611e+02	112	1.5417590e+02	113	1.4665669e+02
114	1.3950420e+02	115	1.3270050e+02	116	1.2622860e+02
117	1.2055360e+02	118	1.1757710e+02	119	1.1652370e+02
120	1.1547970e+02	121	1.1285390e+02	122	1.1028790e+02
123	1.0564610e+02	124	1.0303760e+02	125	1.0211450e+02
126	1.0160520e+02	127	1.0109840e+02	128	1.0059420e+02
129	9.7328743e+01	130	9.3325592e+01	131	8.8774048e+01
132	8.3939339e+01	133	7.9367928e+01	134	7.6332161e+01
135	7.3559479e+01	136	7.1886917e+01	137	6.9068199e+01
138	6.6826141e+01	139	6.6492851e+01	140	6.6161209e+01
141	6.5831230e+01	142	6.5502899e+01	143	6.5045982e+01
144	6.4592247e+01	145	6.3630589e+01	146	6.2308281e+01
147	5.9925030e+01	148	5.7059490e+01	149	5.4059990e+01
150	5.2989529e+01	151	5.1784679e+01	152	4.9259110e+01
153	4.7517319e+01	154	4.6205292e+01	155	4.5290371e+01
156	4.4172138e+01	157	4.3124630e+01	158	4.2144089e+01
159	4.1227039e+01	160	3.9729511e+01	161	3.8787361e+01
162	3.7791882e+01	163	3.7303768e+01	164	3.6858799e+01
165	3.6419140e+01	166	3.6056759e+01	167	3.5697990e+01
168	3.4539181e+01	169	3.3085468e+01	170	3.1692949e+01
171	2.7885151e+01	172	2.4657829e+01	173	2.2535561e+01
174	2.2378361e+01	175	2.2155689e+01	176	2.2001141e+01
177	2.1701780e+01	178	2.1485849e+01	179	2.1335970e+01
180	2.1229561e+01	181	2.1144810e+01	182	2.1060400e+01
183	2.0976320e+01	184	2.0767611e+01	185	2.0684700e+01
186	2.0602131e+01	187	2.0519880e+01	188	2.0417540e+01
189	2.0275120e+01	190	2.0073380e+01	191	1.9597349e+01
192	1.9392651e+01	193	1.9199690e+01	194	1.9084841e+01
195	1.7959049e+01	196	1.7759029e+01	197	1.7564760e+01
198	1.7445721e+01	199	1.6830530e+01	200	1.6550140e+01
201	1.6049770e+01	202	1.5779230e+01	203	1.4866260e+01
204	1.4730120e+01	205	1.4595220e+01	206	1.4470240e+01
207	1.4250530e+01	208	1.4049610e+01	209	1.3546040e+01
210	1.3329701e+01	211	1.2599970e+01	212	1.2472100e+01
213	1.2308550e+01	214	1.2130150e+01	215	1.1979470e+01
216	1.1815291e+01	217	1.1709430e+01	218	1.1589440e+01
219	1.1269440e+01	220	1.1052920e+01	221	1.0803760e+01

222	1.0579250e+01	223	9.5000238e+00	224	9.1403112e+00
225	8.9799500e+00	226	8.8003750e+00	227	8.6736898e+00
228	8.5240736e+00	229	8.3003216e+00	230	8.1302719e+00
231	7.9700790e+00	232	7.8396511e+00	233	7.7399430e+00
234	7.6003499e+00	235	7.3801532e+00	236	7.1398692e+00
237	6.9942918e+00	238	6.9177761e+00	239	6.8702078e+00
240	6.8352590e+00	241	6.8106961e+00	242	6.7916532e+00
243	6.7760501e+00	244	6.7598071e+00	245	6.7422538e+00
246	6.7166829e+00	247	6.6312571e+00	248	6.6061058e+00
249	6.5882931e+00	250	6.5718432e+00	251	6.5560899e+00
252	6.5390658e+00	253	6.5149159e+00	254	6.4817748e+00
255	6.4320569e+00	256	6.3597841e+00	257	6.2801528e+00
258	6.1601081e+00	259	6.0599060e+00	260	5.9601421e+00
261	5.8002110e+00	262	5.7201462e+00	263	5.6197901e+00
264	5.5300360e+00	265	5.4881668e+00	266	5.4102449e+00
267	5.3800321e+00	268	5.3201122e+00	269	5.2100759e+00
270	5.1099739e+00	271	4.9332318e+00	272	4.7678452e+00
273	4.4197998e+00	274	4.3098121e+00	275	4.2198281e+00
276	4.0000000e+00	277	3.8821700e+00	278	3.7120869e+00
279	3.5430729e+00	280	3.1421089e+00	281	2.8840470e+00
282	2.7751210e+00	283	2.7409220e+00	284	2.7198980e+00
285	2.7001150e+00	286	2.6400411e+00	287	2.6200531e+00
288	2.5900941e+00	289	2.5500031e+00	290	2.4699409e+00
291	2.3300610e+00	292	2.2729859e+00	293	2.2170870e+00
294	2.1569481e+00	295	2.0700951e+00	296	1.9899200e+00
297	1.9000770e+00	298	1.7799660e+00	299	1.6689490e+00
300	1.5880300e+00	301	1.5199760e+00	302	1.4439670e+00
303	1.4100070e+00	304	1.3809810e+00	305	1.3309521e+00
306	1.2930380e+00	307	1.2509390e+00	308	1.2139680e+00
309	1.1699890e+00	310	1.1479690e+00	311	1.1299740e+00
312	1.1160491e+00	313	1.1039500e+00	314	1.0919820e+00
315	1.0779860e+00	316	1.0349931e+00	317	1.0210120e+00
318	1.0090350e+00	319	9.9650049e-01	320	9.8195911e-01
321	9.6395981e-01	322	9.4402218e-01	323	9.1997790e-01
324	8.8002437e-01	325	8.2003713e-01	326	7.1999890e-01
327	6.2499869e-01	328	5.9499300e-01	329	5.5498970e-01
330	5.2001083e-01	331	4.7501651e-01	332	4.3157861e-01
333	3.9000109e-01	334	3.5299349e-01	335	3.2500789e-01
336	3.0501151e-01	337	2.7998880e-01	338	2.5499651e-01
339	2.3119231e-01	340	2.0961019e-01	341	1.9000490e-01
342	1.6189531e-01	343	1.3799940e-01	344	1.1999490e-01
345	1.0429770e-01	346	8.9796834e-02	347	7.6496862e-02
348	6.5199360e-02	349	5.5498149e-02	350	4.7301859e-02
351	4.0299930e-02	352	3.4399759e-02	353	2.9298890e-02
354	2.4939420e-02	355	2.0010350e-02	356	1.4829960e-02
357	1.0450500e-02	358	7.1452628e-03	359	4.5560212e-03
360	2.4998970e-03	361	1.1000270e-04		

# Appendix C

## NJOY Inputs

Sample NJOY input files are given here. Included are inputs for H-1 ( $H_2O$ ), O-16, U-235, and U-238. For all inputs presented here, the SHEM361 group structure is used. The group boundary listings are incomplete for brevity.

### C.1 H-1

```
moder
 20 -21

moder
 59 -58

reconr
 -21 -22
 'pendf tape for H-H2O'/
 125 1/
 0.001 0. 0.005/
 'H-H2O point-wise ENDF tape'/
 0/

broadr
 -21 -22 -23
 125 1/
 0.001/
 2.936E+02/
 0/

thermr
 -58 -23 -35
 1 125 16 1 4 0 2 222 0/
 2.936E+02/
 0.001 4.0

groupr
```

```
-21 -35 0 -26
125 1 0 4 0 1 1 1
'H-H2O for for UF14768 library'/
2.936E+02/
1.0E+10/
361 /
1.1000270E-04
2.4998970E-03
4.5560212E-03
[ ... ]
1.3840290E+07
1.4918230E+07
1.9640300E+07 /

0.2 0.0253 820.3E+3 1.40E+6 / iwt=4 parameters
3/
3 222/
6/
6 222/
0/
0/

moder
-26 30

stop
```

## C.2 O-16

```
moder
20 -21

reconr
-21 -22
'pendf tape for 016'
825 1/
0.001 0. 0.005/
'016 point-wise ENDF tape' /
0/

broadr
-21 -22 -23
825 1/
0.001/
2.936000E+02/
0/

thermr
0 -23 -35
0 825 16 1 1 0 1 221 0
2.936000E+02/
0.001 4.0

groupr
-21 -35 0 -26
825 1 0 4 0 1 1 1
'016 for UF14768 library' /
2.936000E+02/
1.0e10/
361 /
1.1000270E-04
2.4998970E-03
4.5560212E-03
[ ... ]
1.3840290E+07
1.4918230E+07
1.9640300E+07 /

0.2 0.0253 820.3e3 1.40e6 / iwt=4 parameters

3/
3 221 /

6 /
6 221 /
0/

0/

moder
-26 30
stop
```

### C.3 U-235

```
moder
20 -21

reconr
-21 -22
'pendf tape for U235'/
9228 1/
0.001 0. 0.005/
'U235 point-wise ENDF tape' /
0/

broadr
-21 -22 -23
9228 1/
0.001/
293.6/
0/

thermr
0 -23 -35
0 9228 16 1 1 0 1 221 0
293.6/
0.001 4.0

groupn
-21 -35 0 -26
9228 1 0 4 0 1 1 1
'U235 for SHEM361 library' /
293.6/
1.0e10/
361 /
1.1000270E-04
2.4998970E-03
4.5560212E-03
[ ... ]
1.3840290E+07
1.4918230E+07
1.9640300E+07 /

0.2 0.0253 820.3e3 1.40e6 / iwt=4 parameters

3/
3 221 /
3 452 /
3 455 /
5 455 /
6 /
6 221 /
0/

0/

moder
-26 30
stop
```

## C.4 U-238

```
moder
20 -21

reconr
-21 -22
'pendf tape for U238'/
9237 1/
0.001 0. 0.005/
'U238 point-wise ENDF tape' /
0/

broadr
-21 -22 -23
9237 1/
0.001/
293.6/
0/

thermr
0 -23 -35
0 9237 16 1 1 0 1 221 0
293.6/
0.001 4.0

groupr
-21 -35 0 -26
9237 1 0 4 0 1 1 1
'U235 for SHEM361 library' /
293.6/
1.0e10/
361 /
1.1000270E-04
2.4998970E-03
4.5560212E-03
[ ... ]
1.3840290E+07
1.4918230E+07
1.9640300E+07 /

0.2 0.0253 820.3e3 1.40e6 / iwt=4 parameters

3/
3 221 /
3 452 /
3 455 /
5 455 /
6 /
6 221 /
0/

0/

moder
-26 30
stop
```